

Citation for published version:

Martins, K, Blenkinsopp, C, Almar, R & Zang, J 2017, 'The influence of swash-based reflection on surf zone hydrodynamics: a wave-by-wave approach', *Coastal Engineering*, vol. 122, pp. 27-43.
<https://doi.org/10.1016/j.coastaleng.2017.01.006>

DOI:

[10.1016/j.coastaleng.2017.01.006](https://doi.org/10.1016/j.coastaleng.2017.01.006)

Publication date:

2017

Document Version

Peer reviewed version

[Link to publication](#)

Publisher Rights

Unspecified

The raw model data and OpenFOAM setup files created during this research are openly available from the University of Bath data archive at <https://doi.org/10.15125/BATH-00466>.

University of Bath

Alternative formats

If you require this document in an alternative format, please contact:
openaccess@bath.ac.uk

General rights

Copyright and moral rights for the publications made accessible in the public portal are retained by the authors and/or other copyright owners and it is a condition of accessing publications that users recognise and abide by the legal requirements associated with these rights.

Take down policy

If you believe that this document breaches copyright please contact us providing details, and we will remove access to the work immediately and investigate your claim.

The influence of swash-based reflection on surf zone hydrodynamics: a wave-by-wave approach

Kévin Martins^{1*}, Chris E. Blenkinsopp¹, Rafael Almar², Jun Zang¹

¹*Research Unit for Water, Environment and Infrastructure Resilience (WEIR), Department of Architecture and Civil Engineering, University of Bath, Claverton Down Road, Bath, BA2 7AY, UK*

²*LEGOS (CNRS/CNES/IRD/Université de Toulouse), Toulouse, France*

Abstract

A detailed understanding of the behaviour of waves in the nearshore is essential for coastal engineers as these waves cause beach erosion, coastal flooding and damage to coastal structures. Significantly, the influence of reflected waves is often neglected in surf zone studies, although they are known to influence wave properties and circulation in the nearshore. In this paper, a phase-resolving model is rigorously applied to model conditions from the prototype-scale BARDEXII experiment in order to examine and assess the influence of swash-based reflection on surf zone hydrodynamics at both the individual wave and time-averaged timescales. Surface elevation is separated into incoming and outgoing signals using the Radon Transform and a crest tracking algorithm is used to extract incident and reflected wave properties. It is found that on steep beaches ($\tan \beta > 1 : 9$) the swash-based reflection - the reflection generated in the swash during the backwash - contributes significantly to the intrawave variability of individual wave properties such as the wave height to water depth ratio γ , through the generation of quasi-nodes/antinodes system. For γ expressed with individual wave heights, variations up to 25% and 40% are obtained for the modelled regular and irregular wave tests, whereas it reaches 15% when it

*Corresponding author

Email addresses: K.Martins@bath.ac.uk (Kévin Martins^{1*}), C.Blenkinsopp@bath.ac.uk (Chris E. Blenkinsopp¹), rafael.almar@ird.fr (Rafael Almar²), j.zang@bath.ac.uk (Jun Zang¹)

is based on the significant wave height. The outgoing wave field-induced hydrodynamics is also found to affect time-averaged parameters: undertow and horizontal velocity skewness. The undertow is mainly strengthened, particularly in the shoaling region where the outgoing component dominates over the contribution from the incoming wave field. Offshore of the bar, an onshore-directed flow streaming close to the bed is also generated under the outgoing wave field, and is suspected to help in stabilising the bar position. This, along with the influence of the outgoing wave field on the horizontal velocity skewness and the presence of quasi-standing waves, suggests a complex contribution of the hydrodynamics induced by swash-based reflection into sediment transport rates and nearshore bar generation/migration.

Keywords: CFD; OpenFOAM®; Surf zone; prototype laboratory experiments; swash-based reflection; Radon transform; wave-by-wave approach

1. Introduction

Wave reflection from beaches and other coastal features is known to influence incident wave-induced hydrodynamics and therefore morphodynamics [1, 2].

While there are many studies of structure-induced reflection present in the literature (see Zanuttigh and van der Meer [3], for a relatively recent comparison of extensive datasets), it is evident that prior studies focusing on wave reflection from natural beaches, especially in the sea/swell band ($0.05 \text{ Hz} \leq f \leq 0.5 \text{ Hz}$), are relatively limited. The reflection of monochromatic waves over a slope was first investigated by Iribarren and Nogales [4], and Miche [5] and it has been shown that the reflection coefficient of a slope, defined as the ratio between incident and reflected wave height $K = H_r/H_i$, is linked to the surf-similarity parameter [6]:

$$\xi = \tan \beta / \sqrt{H_o/L_o} \quad (1)$$

where β is the structure or beach slope, and H_o and L_o are the offshore wave height and wavelength, respectively. While the reflected wave phase was found

15 to be only dependent on the offshore wave steepness and the slope [7], the ampli-
 16 tude of reflected waves are substantially influenced by the bottom roughness and
 17 permeability, but also the nature of wave transformation across the surf zone
 18 (Battjes [6], Hughes and Fowler [7], Miles and Russell [8] and many others).
 19 By presenting cross-shore varying reflection coefficients from two field-based ex-
 20 perimental datasets, Baquerizo et al. [9] observed a net increase in reflection
 21 coefficients shoreward of the break point, and suggested that when defining the
 22 reflection coefficient of a beach, it should be measured as far offshore as possi-
 23 ble. Although this approach is appropriate for studying the bulk outgoing wave
 24 energy from a beach, it presents several issues. Assessing the outgoing energy
 25 further from shore increases the risk of observing additional phenomenon, par-
 26 ticularly from non-linear wave interactions [10, 11], that can lead to reflection
 27 coefficients higher than unity [12]. Furthermore and as discussed by Battjes [6],
 28 based on the methodology of Miche [5], the processes responsible for incident
 29 wave energy dissipation in the surf zone (mainly friction and breaking) have to
 30 be approximated, while a measurement close to the swash zone would lead to an
 31 exact estimation of reflected waves (height and phase), using the local incident
 32 properties.

33 In the few field-based studies focusing on wave reflection in the sea/swell
 34 range of frequencies, it was generally demonstrated that reflection could be
 35 substantial [13, 8, 14]. Using an array of 24 bottom-mounted pressure sensors,
 36 Elgar et al. [13] found that up to 18% of the incident sea-swell frequency band
 37 was reflected back into the surf zone. These relatively high levels of reflected
 38 energy in the surf affect the incident waves in a variety of ways. Fluctuations
 39 in the currents velocities due to the reflected wave orbital velocities influence
 40 the sediment suspension [1], also potentially influencing the velocity skewness,
 41 important for onshore sediment transport [15, 16]. Instantaneous sea levels are
 42 also influenced by the presence of seaward propagating wave crests and troughs,
 43 which influence the wave height to depth ratio γ , due to the presence of quasi-
 44 standing waves [17]. Many parameterisations are present in the literature to
 45 describe the cross-shore variation of this wave parameter, related to the wave

energy dissipation (see for example the pioneering work of Battjes and Janssen [18]). While existing parameterisations of γ do not explicitly account for wave reflection, both γ and reflection are a function of beach slope and wave number [19, 20, 21]. It is known that the beach slope controls the wave reflection to a great extent (see above, and Almar et al. [14, 22]). Through observation of the influence of strong backwash flows on the generation of individual reflected waves at the surf-swash boundary, a link might be expected between reflected waves generated by swash flows and the wave height to water depth ratio of individual waves in the surf zone, though no evidence is present in the literature.

A lack of field-based studies of sea/swell reflection on beaches can be explained by the complexity in measuring the energy bulk reflected from a beach-face. Several methods to separate incoming from outgoing wave fields exist; see for example Inch et al. [23] for a recent description. Correlation functions between 2 wave gauges were used (Kajima [24], Thornton and Calhoun [25] in Goda and Suzuki [26]) before Goda and Suzuki [26] introduced the use of Fast-Fourier Transform (FFT) to speed up this process. This was later extended to a larger array of wave gauges - see for example Mansard and Funke [27], Zelt and Skjelbreia [28] or Lin and Huang [29] - which enables the error in the separation process to be reduced [23]. Other methods such as PUV (Pressure, U horizontal and V vertical current velocities, Guza and Bowen [30]), or approaches based on long-wave theory described in Guza et al. [31] use collocated pressure or surface elevation signals, and horizontal current velocities to separate incoming and outgoing signals at a cross-shore location. Using a totally different approach, Almar et al. [32] describe the use of the Radon Transform (RT) for nearshore wave studies, with the objective of finding tools to facilitate wave-by-wave analyses. Mostly used in image processing, the RT can be applied to the projection of a cross-shore/temporal diagram $\eta(x, t)$ into points in the Radon (polar) space. This method is therefore particularly suitable in the surf zone as with increasing non-linearities, the wave tracks appear as well-defined lines in such diagrams (*e.g.* Almar et al. [33]). Almar et al. [32] successfully separated incident and reflected long-wave signals from a laboratory dataset

77 and demonstrated that the results compared well with those from a Boussinesq
78 model.

79 In this study, the RT is applied to the results from a phase-resolving nu-
80 merical model simulating two monochromatic and one irregular wave tests, per-
81 formed at prototype-scale in the Delta flume during the BARDEXII project
82 [34]. The primary objective is to study the impact of reflected waves on inci-
83 dent wave properties and surf hydrodynamics with a focus on sea/swell waves.
84 For irregular waves, the free surface is actually a sum of wave trains, with dif-
85 ferent frequency and possibly direction (incident and reflected). In this regard,
86 a wave-by-wave approach is developed based on the previous work of Martins
87 et al. [21], allowing individual wave tracking from the shoaling area to the runup
88 limit, and back into the flume after reflection.

89 The paper is organised as follows. Section 2 introduces the experimental
90 and numerical datasets. The numerical model is validated using a large ar-
91 ray of instruments, including a Terrestrial Laser Scanner (TLS) that enables
92 the description of the wave shape during breaking. The signal separation in
93 incoming/outgoing components and the wave-by-wave approach used to track
94 individual wave properties are described in Section 3. Section 4 presents the
95 results on the separation methods and its application for the study of swash-
96 based reflection influence on surf zone hydrodynamics at the individual wave
97 timescale. The concept of swash-based reflection is notably explained through
98 a link with swash events potential energy. The results and the influence of re-
99 flection at longer timescales are then discussed in Section 5. Finally Section 6
100 provides the conclusions of this study.

101 **2. Experimental and numerical datasets**

102 *2.1. The BARDEXII experiments*

103 The present study uses experimental data obtained during the 2-month-long
104 BARDEXII experiment [34]. In order to study wave processes and cross-shore
105 sediment transport in the surf and swash zones, a coarse sandy beach/barrier

106 system was built in the prototype-scale Delta Flume (Vollenhove, The Nether-
 107 lands). The A6 and A7 monochromatic test cases (hereafter A6-mono and
 108 A7-mono) and A6-01 irregular wave test are the focus of the present study
 109 [34]. Regular second-order Stokes waves were generated during the the A6-
 110 mono and A7-mono tests by a second-order wave steering system at $x = 0$ m,
 111 with an Active Reflection Compensation system (ARC) for the absorption of
 112 reflected waves. For the A6-01 irregular test, a JONSWAP spectrum with a
 113 peak enhancement factor of 3.3, was imposed in the wave flume. The initial
 114 beach profile of 1 : 15 slope between $x = 49 - 109$ m evolved under the wave
 115 action during Series A1 to A7 to result in the bed profiles presented in Figure
 116 1, presenting a much steeper upper beach face, a bar system for the A6-01 and
 117 A6-mono, and a terrace for the A7-mono. The wave forcing conditions and
 118 beach slope for the different wave tests examined here are presented in Table 1.

119 A large array of instrumentation was used during the experiments, and only
 120 part of the experimental dataset is used to validate the numerical model used
 121 herein. The positions of the instruments used in the present work are shown in
 122 Figure 1. A series of pressure transducers (PT) and electro-magnetic current
 123 meters (EMCM) both sampled at 20 Hz were located in the shoaling and surf
 124 zones to measure the pressure and flow velocity under propagating and breaking
 125 waves. Two terrestrial laser scanners were deployed to measure free surface
 126 elevations within the flume, the first was positioned in the surf zone at $x =$
 127 73.6 m, 3.9 m above mean sea level (MSL) while the second was deployed at
 128 $x = 88.3$ m, 3.8 m above MSL to study the swash zone hydrodynamics and
 129 morphodynamics. The TLS recorded data at an angular resolution of 0.25°
 130 and sample rate of 35 Hz; the measurements were processed following Martins
 131 et al. [21] including the correction of the scanner orientation, noise filtering and
 132 spatial interpolation onto a regular grid.

133 TLS data is ideal for wave-by-wave analysis of surf zone processes as the high-
 134 spatial and temporal resolutions of the measurements allow for the description
 135 of wave geometry and the tracking of individual wave properties through hun-
 136 dreds of cross-shore positions. Physical constraints within the flume limited the

137 elevation of the TLS and hence the horizontal extent of the measurements, how-
 138 ever the high resolution of the data enabled the wave shape to be captured in the
 139 swash zone and around the primary break point for detailed model validation.

140 The PT data were used to retrieve the surface elevation using the linear wave
 141 theory, and the classic pressure response factor (see *e.g.* Bishop and Donelan
 142 [35]):

$$K_p = \frac{\cosh(k(\bar{h} + z))}{k\bar{h}} \quad (2)$$

143 where \bar{h} is the mean water depth, k is the radian wavenumber and z the PT
 144 deployment depth. The methodology described by Inch [36] was followed, using
 145 the high frequency cut-off $w_c = 0.564\pi\sqrt{g/\bar{h}}$ (where g is gravity) proposed in
 146 Green [37], to prevent noise amplification. Correcting the signal depth attenua-
 147 tion with linear wave theory is known to lead to an underestimation of the wave
 148 crest elevation, especially for highly non-linear waves, see for instance Nielsen
 149 [38], Townsend and Fenton [39] or Barker and Sobey [40]. Bishop and Donelan
 150 [35] suggested that wave heights could be retrieved within 5%, but no estimation
 151 based on wave-by-wave analysis has ever been carried out, thus the impact of
 152 the correction at this time scale is unknown. For that reason, the differences at
 153 the wave-by-wave scale between the TLS and PT datasets were assessed prior
 154 to any model validation.

155 Figure 2a shows the wave profiles measured at $x = 72.5$ m, close to the
 156 break point, by both instruments for every wave of the A7-mono test case and
 157 its ensemble-average, with the modelled surface elevation also shown. In this
 158 study, the break point is defined as the point of maximum wave height; for this
 159 comparison it was assessed from the wave height evolution (TLS), comparisons
 160 between model and data presented further in this paper, and from video data
 161 (not shown here) in order to exclude the presence of foam that could increase
 162 discrepancies between datasets. It is demonstrated that at the early stage of
 163 breaking, the individual wave height is underestimated by approximately 30%.
 164 Additionally, considerable differences are observed in the two wave shapes (skew-
 165 ness and steepness): wave non-linearities at the wave-by-wave scale are largely

underestimated when using the linear theory to retrieve the surface elevation. For these reasons, the raw pressure signals along the wave flume were used to validate the model. Figure 2b shows the ratio of the measured raw pressure to hydrostatic pressure, based on the surface elevation measured by the TLS. It is observed that the two estimates differ significantly before the wave crest where the pressure is higher than hydrostatic and at the crest location, where the measured pressure is well below hydrostatic; a result consistent with previous experimental datasets [41].

Closer to shore, an array of 45 ultrasonic bed level sensors (BLS, see Figure 1 for locations) were deployed in the swash zone to measure water depths and monitor high-frequency bed level changes [42]. Sampling at 4Hz, the BLS are able to measure water depths and bed-level changes using acoustic signals with an accuracy of the order of 1 millimetre. Finally, an ARGUS video camera system was deployed above the beach, in order to monitor surf, swash and overwash processes. In this study, timestacks from the swash camera were used to track the instantaneous shoreline position for comparison with the simulated results.

2.2. Numerical model: IHFOAM [43]

The IHFOAM model [43], based on the CFD package OpenFOAM® (v2.1.1 in the present study) was used to generate waves and simulate their propagation across the wave flume. A library for the wave generation and absorption at boundaries was implemented and the solver modified accordingly. The RANS equations described in Higuera et al. [43] are solved using a VOF (Volume-of-Fluid) method to describe and track the free surface. A rectangular 2D computational mesh for each run was constructed based on survey data, using a cross-shore spacing of $dx = 0.05$ cm and a varying dz , corresponding to a grid of $2100 \times 60 = 126000$ cells. The 2D mesh was manually created using the '.msh' format based on the window-averaged profile, so that no abrupt changes occur near the bed (see Figure 3a). It was then transformed into the OpenFOAM format using the *gmshtofoam* built-in function. The number of

vertical layers was chosen such that the cell aspect ratio was approximately unity near the breaking zone (Figure 3b) to more accurately resolve the break point [44]. Sensitivity testing enabled the mesh size to be optimised to obtain a good compromise between CPU time and precision. A desktop PC with 8 Gb of RAM and a 3.20 GHz quad-core processor was used to run the simulation, with a typical time step of 0.0005 s, varying to fulfil the CourantFriedrichsLewy (CFL) local restrictions. For an 80 second run, this corresponded to approximately 53 hours of CPU time.

Boundary conditions at the wave paddle were generated using second-order Stokes theory [45] for the A6 and A7 monochromatic wave cases. The A6-01 irregular wave case was generated using the actual wavemaker signal (paddle displacement and surface elevation). The active absorption at the wave paddle (located at $x = 0$, see Figure 1) was activated as the Delta flume is equipped with an ARC system, preventing radiated components from being re-reflected towards the artificial beach.

The VOF-based CFD method attributes an α value to the typically two modelled phases of interest, for instance air and water [46]. A cell containing only water corresponds to $\alpha = 1$, whereas a cell filled with air corresponds to $\alpha = 0$. The free surface was extracted by integrating α over the water column at a given position. This method is considered particularly suitable for spilling or weakly plunging waves, characterized by relatively low air entrainment. Finally, the $k - \omega$ SST turbulence closure model developed by Menter [47] was used as it was found to better reproduce the surface elevation than the classical $k - \epsilon$ and $k - \omega$ models [48]. For further details on the model equations, the reader is referred to Higuera et al. [43].

2.3. Validation of the numerical model

2.3.1. Surface elevation and relative pressure in the surf zone

The detailed surface elevation measurements from the TLS and ultrasonic BLS were used to validate the model predictions of free surface elevation around the break point. Figure 4 shows instantaneous comparisons between the TLS

226 and BLS measurements and the modelled water phase for the A7-mono test
 227 case at 6 times during the breaking process. Comparisons show good agreement
 228 ($\text{RSME} < 0.06 \text{ m}$, $r^2 > 0.96$) at every stage of the breaking (wave shape evolution
 229 and breaking location), with the modelled free surface closely capturing the
 230 complex wave geometry resolved from hundreds of point measurements obtained
 231 by the TLS. Despite this good model agreement in mean errors (Table 2), the
 232 existence of short duration, low void fraction, but large magnitude splashes
 233 generated during breaking (landward of $x = 76 \text{ m}$, see Figure 4d) lead to large
 234 maximum errors (MAE). These splashes are captured by the TLS once the wave
 235 crest propagates landward of $x = 76 \text{ m}$ but are not expected to be resolved by
 236 the CFD model. In opposition, the significant MAE observed for the PT (Table
 237 2) are due to the poor performance of linear theory to retrieve the surface
 238 elevation at this location (Figure 2).

239 To validate the modelled wave transformation across the wave flume the
 240 modelled relative pressure was compared with the raw pressure data from the
 241 PTs. For conciseness, only results for the 670s-long A6-01 irregular wave test are
 242 shown; the statistical errors from all tests are shown in Table 2. Figure 5 shows
 243 a 360 second window of the modelled and measured relative pressure timeseries
 244 from the shoaling area to the surf zone. The transformation of the incident waves
 245 is well described by the model ($\text{RMSE} = 0.02 - 0.04 \text{ dbar}$ and $r^2 = 0.92 - 0.97$),
 246 with a good representation of the wave profile changes. Though it is less clear
 247 than from a surface elevation timeseries, the more tooth-shaped wave profile
 248 after breaking (from $x = 72.5 \text{ m}$) can clearly be seen. These comparisons show
 249 the potential of using the piston-type boundary conditions to generate irregular
 250 wave trains in prototype-scale experiments.

251 *2.3.2. Surf and the swash hydrodynamics*

252 Horizontal and vertical current velocities were measured at various cross-
 253 shore locations along the wave flume (see Figure 1). These measurements were
 254 used to validate the modelled wave-induced hydrodynamics in the shoaling and
 255 surf zones. Figure 6 shows comparisons of measured and modelled horizontal

256 and vertical velocities for the A6-01 irregular wave test. Overall, the model
 257 successfully reproduces the wave-induced hydrodynamics through the shoaling
 258 region and surf zone (similar good agreement was found for the regular wave
 259 tests, see Table 2). More specifically, the high-magnitude current velocities
 260 observed after breaking ($x = 77.5$ m) are well described in the numerical model.
 261 Some discrepancies are observed in these comparisons, where measured current
 262 velocities are noisy in some locations, *e.g.* close to the surface at $x = 77.5$ m
 263 and $z = 2.70$ m. These periods occur during the passage of the two largest wave
 264 groups, and could be explained by a high concentration of entrained air bubbles,
 265 which are known to introduce noise when using EMCs (see for example Gailani
 266 and Smith [49], Elgar et al. [50] or Huang and Hwang [51]).

267 As the swash zone is thought to significantly influence surf zone processes
 268 [2], primarily due to its role in reflecting incident wave energy, the ability of
 269 the model to reproduce swash zone processes was assessed. The model results
 270 were compared against measurements of the shoreline position (ARGUS video
 271 camera) and swash depths (BLS and TLS). The cross-shore position of the
 272 shoreline was manually extracted from the video timestacks. The modelled
 273 shoreline was computed using a 3 cm threshold from the modelled water depths.
 274 Both modelled and measured shoreline cross-shore positions were transformed
 275 into a vertical elevation using the surveyed beach profile. Figure 7 shows the
 276 timeseries comparisons of modelled and measured shoreline elevation for the
 277 entire A6-01 test, along with a 2-minute subset of the data comparing cross-
 278 shore shoreline position and swash depths. Although the modelled runup extent
 279 is sometimes slightly overestimated (Figure 7a and 7b), comparisons show very
 280 good agreements between the two datasets. In particular, the timing of the
 281 uprush and downrush phases (Figure 7b) as well as water volumes (7c-e) are
 282 accurately reproduced. Figures 7c-e highlight some pros and cons of different
 283 methods for measuring flow depths in the swash zone (TLS and ultrasonic BLS
 284 in this case). In Figure 7d, it is observed that there are periods, particularly
 285 in the lower swash during backwash where insufficient light is scattered by the
 286 water surface and no signal return is detected by the TLS. Reduced ability to

287 detect water depths during backwash and close to the shoreline is common when
 288 using TLS, and enhanced here by the reduced persistence of aeration observed
 289 in freshwater (*e.g.* Blenkinsopp and Chaplin [52]). This effect means that TLS
 290 measurements tend to underestimate the shoreline position as observed by [53].
 291 By contrast, the measurements from the BLS are much more consistent but are
 292 limited by the much reduced spatial resolution, meaning that the wave/bore
 293 front is less well resolved.

294 **3. Methods**

295 *3.1. Separation of the incoming and outgoing signals*

296 In the present study, the influence of reflected waves was studied at two dis-
 297 tinct timescales: individual wave timescale and time-averaged over a complete
 298 wave test. In order to study the evolution of individual incident wave properties,
 299 the Radon Transform (RT) was applied to the modelled free surface elevation
 300 to separate the incoming and outgoing signals. The RT was successfully ap-
 301 plied to study wave celerity and incident and reflected short and long waves
 302 by Almar et al. [33] and Almar et al. [32]. The method applies the following
 303 transformation [54] to a surface elevation signal $\eta(x, t)$:

$$R(\rho, \theta) = \oint\!\!\!\oint \eta(x, t) \delta(x \cos \theta + t \sin \theta - \rho) dx dt \quad (3)$$

304 where x represents the cross-shore dimension, and t is time, δ is the Dirac
 305 function, ρ and θ the distance and angle from origin of the integration line
 306 defined by $\rho = x \cos \theta + t \sin \theta$ [32]. As described in Almar et al. [32], lines in
 307 the Cartesian spatio-temporal space ($\eta(x, t)$ diagram) are represented by points
 308 in the Radon space.

309 More interestingly for the present study, when a wave reflects off the beach,
 310 it is also visible as a line in the aforementioned $\eta(x, t)$ diagram. By integrating
 311 the Radon signal over the correct angles with the inverse RT [32], the separation
 312 of the incoming and outgoing signals is made possible. The result enables the

313 modelled surface elevation to be described as:

$$\eta(x, t) = \eta_{inc}(x, t) + \eta_{out}(x, t) \quad (4)$$

314 where the '*inc*' and '*out*' subscripts refer to the incoming and outgoing com-
315 ponents respectively. An example of this process is shown in Figure 8 for the
316 A7-mono test which demonstrates the strength of this method: incident (Figure
317 8b) and reflected waves (Figure 8c) clearly appear as lines in the $\eta(x, t)$ diagram.
318 Note that in this study, a difference is made between 'reflected' wave and 'out-
319 going' signal. While at the wave-by-wave time scale it is evident that the wave
320 propagating seaward from the beach upper slope is generated through reflection,
321 it is not clear how other signals propagating seaward are originated, especially
322 at longer time scales (*e.g.* non-linear interactions). The term 'reflected wave'
323 is therefore only used to describe seaward propagating waves generated at the
324 boundary between the swash backwash and the inner surf that can be tracked
325 (swash-based reflection). The same reasoning is applied to differentiate 'inci-
326 dent' wave from 'incoming' signal.

327 The separation based on the RT was compared in the frequency domain to
328 the commonly used method of Guza et al. [31] (hereafter Guza84). The Guza84
329 method was developed from long-wave theory and uses collocated surface el-
330 evation and horizontal current velocities signals to separate the incoming and
331 outgoing components of surface elevation or horizontal current velocities. The
332 use of this linear theory-based method is motivated by two reasons: 1) a per-
333 formance comparison with the RT to assess the model capacity in reproducing
334 the wave spectra and 2) the observed poor performance of the RT to resolve
335 mean flow velocities after separation. While the RT was found to satisfacto-
336 rily separate incoming and outgoing signals (for both η and u), mean incoming
337 and outgoing cross-shore flow velocities close to zero were found when time-
338 averaged. The two possible explanations are the introduction of noise in the
339 high frequencies, which makes the average of the whole signal tend to zero, or
340 the less sharp 'lines' in the $u(x, t)$ diagram, compared to the $\eta(x, t)$ diagram
341 observable in Figure 8a.

342 For this reason, linear theory was used to separate surface elevation and
 343 horizontal current velocity in order to study the influence of reflection on time-
 344 averaged surf zone parameters (undertow, wave setup and horizontal velocity
 345 skewness). Modelled horizontal current velocities were extracted from the re-
 346 sults of the A6-01 test along the wave flume at various heights above the bed
 347 ranging from 0.01 m to 1.8 m (non-dimensional height $z' = z/\bar{h} \in [0, 0.6]$) using
 348 the Guza84 method [55]. After performing the aforementioned current separa-
 349 tion, horizontal current velocities were averaged over the entire test to compute
 350 the mean cross-shore current velocities (undertow) and velocity skewness defined
 351 as $S_k = \overline{u^3}/\overline{u^2}^{3/2}$, where $\overline{\cdot}$ is the time-averaging operator.

352 3.2. Wave-by-wave approach

353 The results at the individual wave timescale presented in this paper rely
 354 on a wave-by-wave analysis, performed separately on the extracted incoming
 355 and outgoing signals. At every cross-shore position between $x = 0$ and 84 m,
 356 local peaks in the surface elevation timeseries (corresponding to wave crests)
 357 are identified to enable the extraction of individual wave properties (*e.g.* H, T),
 358 following an improved version of the methodology presented in Martins et al.
 359 [21]. Previous work has been undertaken to study individual wave properties;
 360 see for example recent studies of Power et al. [56, 57], Postacchini and Brocchini
 361 [58]. These methods are based on peak-to-peak analysis which bypasses the need
 362 for low-pass filtering but cannot deal with the superposition of waves travelling
 363 in either the same or opposing directions.

364 The present algorithm starts by extracting wave properties at an initial cross-
 365 shore position (*e.g.* $x = 0$ m, for incident waves) using peak analysis: wave crests
 366 are detected and wave troughs are defined as the minimum reached between two
 367 crests. Wave height H is then defined as the height difference between crest and
 368 trough levels, and the wave period T corresponds to the time between the two
 369 troughs surrounding this wave crest. From this initial position, every detected
 370 wave (or a manually-selected subset) can be tracked. At each new cross-shore
 371 position, the time of wave crest detection at the previous cross-shore position is

372 compared to the detection time at the new location. If a wave crest is detected
 373 within a reasonable physical range (based on wave celerity), it is kept as the new
 374 position. If no value is found, wave tracking is ceased. The same methodology
 375 can be applied to both incoming and outgoing signals, with the values for the
 376 physical range set accordingly. The result of this wave tracking algorithm on
 377 the A7-mono test is shown in Figure 8.

378 Using two separate analyses, this methodology was performed on the total
 379 $\eta(x, t)$ and incoming $\eta_{inc}(x, t)$ signals. The following individual wave properties
 380 were extracted: crest height C , wave height H , period T , and depth under pre-
 381 ceding trough h_{tr} . The analysis performed on the incoming signal allows for the
 382 retrieval of incident wave properties, by removing the effect/component of re-
 383 flected waves from the total signal. Reflected wave properties were also extracted
 384 from the outgoing $\eta_{out}(x, t)$ signal in order to assess the incoming/outgoing en-
 385 ergy ratio and study their characteristics as a function of the incident wave
 386 properties.

387 4. Results

388 4.1. Inter-comparison of separation methods

389 Model and experimental data from the A6-01 irregular wave test were com-
 390 pared in the frequency domain by applying the RT on the modelled free surface
 391 elevation and the Guza84 method on the collocated PT/EMCM data. Figure 9
 392 shows the comparison of the total, incoming and outgoing signals at four cross-
 393 shore locations: $x = 42, 67.5, 72.5$ and 77.5 m. At all positions, and for both
 394 sea-swell and infragravity ranges of frequencies, the comparisons show good
 395 agreement. Although the amount of energy is small, more incoming energy at
 396 the infragravity frequencies ($0.005 \text{ Hz} \leq f \leq 0.05 \text{ Hz}$) is estimated in the PT
 397 data at $x = 42$ m (Figure 9b). This could be explained by two factors and it is
 398 not certain which prevails: an underestimation in the model of the transfer of
 399 energy to sub-harmonics between $x = 0$ and 42 m or a more efficient absorption
 400 of outgoing waves at the numerical paddle than in the real flume. The energy

401 peaks and the spectrum tail along the wave flume are well represented every-
 402 where else, indicating that the model is able to simulate the breaking process
 403 and the transfer of energy to higher/lower frequencies. Similar performance has
 404 been observed by Morgan et al. [59] in their modelling of wave transformation
 405 over submerged bar with up to 8th order harmonics correctly simulated.

406 The observed agreement between the RT and the Guza84 approach are some-
 407 what surprising for two main reasons: 1) the previously observed differences at
 408 the wave-by-wave scale between the pressure-derived surface elevation and the
 409 model output close to break point (around 30% of H , Figure 2) is not evident in
 410 the spectral domain, and 2) while the Guza84 method, is thought to be inappro-
 411 priate for use in highly non-linear surf zone waves, the current results indicate
 412 that it can be applied in the surf zone with reasonable results.

413 *4.2. Intrawave variability of wave heights and wave height to water depth ratio*

414 Figure 10a and 10b present the cross-shore evolution of the modelled indi-
 415 vidual wave height H for the total and incoming signals, from the A6-mono
 416 and A7-mono tests. Similar to that observed in the $\eta(x, t)$ diagram presented
 417 in Figure 8a, the reflected components of the waves are clearly observable in
 418 the cross-shore evolution of H . In the total signal $\eta(x, t)$ diagram (Figure 8a),
 419 the first modelled wave after reflection influences the second, third and fourth
 420 incident waves at cross-shore positions of approximately $x = 71$ m, 44 m and
 421 14 m. The surface elevation at these locations is temporarily increased due to
 422 the presence of a reflected wave crest, and this leads to an apparent net increase
 423 in H from total signal at these cross-shore locations, while the values from the
 424 incoming signals obtained from the RT present gradually increasing H values in
 425 the shoaling region, as it should be expected. Similarly, the passage of troughs
 426 also influence H values by decreasing the surface elevation temporarily.

427 The observed effect of reflected waves on individual wave height is also
 428 present in γ values which are expressed as $\gamma = H/\bar{h}$ (Figure 10c and 10d).
 429 Since the first modelled wave is propagating in a calm wave flume, its proper-
 430 ties are not altered by any reflected component: γ_{tot} and γ_{inc} should therefore

431 be similar. This is observed in Figure 10a and 10b where the incoming and
 432 total values match at all positions (gray lines and dots), and in the scatter plots
 433 of Figure 10c and 10d, where gray dots are close to the 1:1 agreement. While
 434 for the subsequent waves in the test there are differences between γ_{tot} and γ_{inc}
 435 values of up to 35% in the shoaling area, this reduces to around 25% closer to
 436 the break point, which is defined as the location of the maximum wave height
 437 for each propagating wave ($x = 71$ m, for both monochromatic tests).

438 A similar wave-by-wave approach was performed for the A6-01 irregular test
 439 case and the results can be observed in Figure 11. Figure 11a shows the cross-
 440 shore evolution of $\gamma_{s,tot}$ and $\gamma_{s,inc}$, based on significant wave height H_s and mean
 441 water depth. In the shoaling area, the two ratios present identical evolution,
 442 demonstrating little influence of reflection on averaged breaker indexes in that
 443 zone. Just offshore of the bar, the values computed from the incoming signals are
 444 slightly larger than those from the total signal, while over the bar the opposite
 445 occurs. The most significant difference is visible on the terrace ($x = 75 - 78$ m),
 446 where incoming values are approximately 15% greater.

447 Individual γ and $\gamma_{tr} = H/h_{tr}$, where h_{tr} is the water depth below the wave
 448 trough, are shown in Figure 11b-e for incoming and total signals. Overall,
 449 the values computed from the incoming signal are less variable; this can be
 450 seen from the slightly smaller error bars and more 'organized' lines, showing
 451 lower intrawave variability. The scatter plots of Figures 11f and 11g allow a
 452 comparison of the different definitions of γ and suggest that variations up to
 453 20% and 40% are common for γ and γ_{tr} respectively which is comparable to
 454 that found for the monochromatic cases (Figure 10c and 10d).

455 The alternate effect of reflected wave crests and troughs on the incident
 456 waves for the irregular wave test is similar to that observed for the monochro-
 457 matic wave tests. This behaviour supports the concept of quasi-standing waves
 458 previously observed by Hoque et al. [17] for shorter waves. The interactions
 459 of two progressive waves travelling in opposite direction, with the same period
 460 but different amplitude (due to wave breaking and friction), generates quasi-
 461 antinodes and quasi-nodes at the location where the incident and reflected waves

are in phase and out of phase respectively. This concept has been investigated for the A6-01 irregular wave test. Figure 12 shows the cross-shore evolution of the ratio of total and incoming variance density spectra $S_\eta/S_{\eta_{inc}}$ for sea/swell frequencies. This ratio indicates the presence of reflected wave energy: a ratio greater than 1 corresponds to the presence of a reflected wave crest, while a ratio lower than 1 corresponds to the presence of a reflected wave trough. For relatively low frequencies ($f \leq 0.2$ Hz), a node/antinode pattern is observed along the wave flume. In particular, for the frequency of the monochromatic wave tests ($f = 0.083$ Hz), a very similar node/antinode system as observed in Figure 10 is found during the irregular wave run: antinodes due to superposed crests are found at around $x = 75$ m, $x = 53$ m and $x = 24$ m, and discrepancies are mainly explained by the different foreshore slope (Table 1). It was suggested for the monochromatic wave tests that partially standing waves were responsible for the intrawave variability of H and hence γ (Figure 10). The results presented in Figure 12 suggest that similar behaviour is observed for irregular waves, and for relatively high frequencies.

4.3. Generation of swash-based reflections

The reflected waves studied here in the sea/swell frequency are thought to be 'generated' primarily by the seaward propagating mass fluxes present in the strong swash backwashes. The term swash-based is therefore used to describe this type of reflection. This concept has been investigated by relating the energy of the tracked reflected waves to the maximum potential energy present in the swash preceding the 'generation' of that reflected wave. The two energy concepts are expressed as follows:

$$E_{ref} = \rho g \int_0^L \eta_{ref}^2(x) dx \quad (5)$$

$$\max_t E_{p,swash}(t) = \rho g \int_0^{R(t)} h(x,t) z(x,t) dx \quad (6)$$

where L is the wavelength, $R(t)$ is the time-varying shoreline position, $h(x,t)$ the water depth and $z(x,t)$ the height above the reference for null potential

energy taken as MSL. In the potential energy formulation from equation 6,
 $z(x, t)$ is the mid flow depth: $z(x, t) = z_{bed}(x) + h(x, t)/2$, where $z_{bed}(x)$ is the
 bed elevation at the cross-shore position x . A sketch describing the terminology
 used in Equation 5 and 6 is presented in Figure 13.

Figure 14 shows the comparison of the two energy expressions for a range of
 both validated and unvalidated test cases. Although not validated in this paper,
 the A1-mono, A2-mono and A4-mono wave tests from the BARDEXII exper-
 iments were run for this investigation in order to have a wider range of beach
 and wave characteristics (see Table 1). Additionally, two further monochromatic
 cases using the same H_s and beach conditions as A7-mono, but with different
 wave periods were modelled (see Table 1). For every regular case, the ensemble-
 averaged energy from the tracked reflected wave (Equation 5, estimated between
 $x = 15$ m and $x = 15 + L$ m) is compared to the ensemble-averaged potential
 energy contained in the preceding swash event ((Equation 6). For the irregular
 run, a subset of 5 individual waves was extracted. For the beach slopes and
 wave conditions examined here, a clear correlation between the two energy for-
 mulations is observed in Figure 14 with the potential energy in a swash event
 consistently double that of the reflected wave that this event generates.

This result suggests that it is possible to estimate the energy and height
 of individual reflected waves based on the monitoring of foreshore bed levels
 and the time-varying surface elevations (leading to water depths and swash
 excursion, the two required parameters). Field deployments of TLS in the swash
 zone such as in Martins et al. [21], Almeida et al. [60] could use this relationship
 to estimate the bulk of energy reflected from the beach. Further investigation
 is required to completely validate this hypothesis, and to explain the presence
 of the 0.5 coefficient of proportionality observed in Figure 14, though this is
 thought to be closely linked to the beach gradient and hence the mass flux in
 the backwash.

516 4.4. Cross-shore evolution of reflection coefficients

517 To the authors' knowledge, Baquerizo et al. [9] were the first to study the
 518 cross-shore variation of the reflection coefficient in the sea/swell range of fre-
 519 quencies, defined as the ratio of incoming and outgoing wave energy. Using
 520 various methods to separate incoming and outgoing signals, they measured in-
 521 creasing reflection coefficient values through the surf zone and suggested that
 522 to minimize the uncertainty introduced by this variation, representative values
 523 should be estimated seaward of the break point. A numerical model based on an
 524 energy balance, taking into account the incident wave dissipation and reflection
 525 from slope was developed by Baquerizo et al. [61] to predict local reflection co-
 526 efficients. Although it showed very good agreement seaward of the break point
 527 it overestimated the reflection coefficient in the surf zone. Discrepancies in the
 528 surf zone are thought to be due to the expression of the reflected wave energy
 529 fluxes, directly linked to the incoming fluxes and the rate of dissipation. To
 530 illustrate this, the energy fluxes defined using linear theory as $F = H^2 c$, where
 531 c is the wave celerity [61], for the incident and reflected waves from the A6-
 532 mono and A7-mono tests are shown in Figure 15a. While the energy fluxes of
 533 reflected waves are approximately constant, meaning that waves are deshoaling
 534 as c increases with increasing depths, the incident waves show a net increase in
 535 energy flux landward of $x = 40 - 50$ m. This occurs when wave celerity cannot
 536 be described anymore by linear wave theory and corresponds to where wave
 537 non-linearities become important (high Ursell number). This overestimation in
 538 the incident wave energy fluxes when non-linearities become significant leads,
 539 for a given dissipation rate, to an overestimation of the reflected wave energy
 540 as defined by Baquerizo et al. [61]. This is consistent with the larger reflected
 541 fluxes found in the surf zone by Baquerizo et al. [9] (see their Figure 8).

542 The direct ratio between incident and reflected individual wave heights is
 543 shown in Figure 15b, for both monochromatic tests. It is shown that up to
 544 the break point ($x = 71$ m), the ratio remains reasonably constant with a slight
 545 decreasing trend for both tests. This is explained by the shoaling incident waves
 546 dominating over the deshoaling reflected waves, observed in Figure 15a. Land-

ward of the break point $x = 71 - 75$ m, and as previously found by Baquerizo et al. [61], the ratio rapidly increases due to the sudden decrease in the wave height after breaking. It is hard to infer from the present dataset what would happen with a wider surf zone and at distances further from the break point. It is natural though to hypothesise an increase of H_{ref}/H_{inc} towards a value which is a function of the wave steepness and the foreshore slope. The energy dissipation rate and the width of the surf zone after break point indeed limit the maximum H_{inc} that can be reflected from a beach, for a given foreshore slope and incident wavelength [5, 6].

5. Discussion

5.1. Break point

The differences observed in the γ values under the presence of reflected waves can be of great significance for numerical models or the parameterisation of wave energy across the surf zone. For instance, a shift seaward or landward of the break point due to the presence of reflected waves will change the energy dissipation patterns across the surf zone, and can affect the position of bar for models supported by the break point hypothesis for sandbar generation [62].

For both monochromatic wave tests, H computed from the total signal reaches its maximum at the same location ($x = 71$ m), see Figure 10a and 10b. However, if only the incoming signal is considered, the maximum wave height is reached around $x = 74$ m for both tests, though it is noted that no strong peak is observed for A7-mono and the wave height remains constant over the low-sloping terrace. If the break point is defined as the location of maximum wave height as used in this study, the results suggest that the incident wave break point occurs further landward. Although no evidence of a direct influence from the reflected wave field on the wave energy dissipation or the breaking onset of incident waves is shown, the detection of the break point with the present definition is affected and therefore biased by the presence of reflected waves.

For the irregular wave test, the presence of reflected waves does not seem to influence the location of the break point as it is observed that the peak values of total and incoming significant wave height computed over sea/swell range of frequencies H_s occur at the same location: $x = 68.5\text{m}$ and $x = 75.4\text{m}$ (Figure 11a). At the inner breakpoint, there is a discrepancy of up to 15% between the gamma values derived from the total and incoming signals and therefore the presence of reflected wave may explain previously observed discrepancies between existing breaker index datasets [63]. Further effort is therefore required to account for the influence of wave reflection on gamma in order to obtain a better description of cross-shore evolution of incident wave height under reflective conditions.

5.2. Influence of wave reflection on time-averaged surf zone parameters

The results presented in Figure 12 suggest that wave reflection in the sea/swell range of frequencies in a reflective environment can influence the surf hydrodynamics at the wave-by-wave scale through the formation of multiple quasi-node/antinode system, affecting orbital velocities. Further influence at longer timescales is discussed here, in terms of undertow, wave setup and horizontal velocity skewness.

5.2.1. Undertow

Horizontal current velocities from the A6-01 test were separated using linear theory (see Section 4.1), and time-averaged to obtain the contribution of both incoming and outgoing wave-induced hydrodynamics on the undertow. Figure 16 shows the result of this separation by illustrating the contribution of the outgoing wave field on the undertow along the wave flume. At the four locations where current velocities measurements are available ($x = 42, 67.5, 72.5$ and 77.5m), modelled mean horizontal flow magnitude is shown against measurements (Figure 16a-d). The ratio $|\overline{U_{out}}|/|\overline{U_{inc}}|$ shown as a contour plot in Figure 16e represents the relative contribution of the outgoing wave field on the mean return flow. Although, over-predicted in the mid-column at $x = 67.5\text{m}$ and slightly underestimated at $x = 77.5\text{m}$, the modelled undertow shows good

604 agreement with data, in terms of magnitude and vertical structure.

605 Consistent with previous work [64], the vertical structure of the undertow
606 evolves with the water depth across the shoaling area and the surf zone. Where
607 non-linearities are small ($\gamma_s \sim O(0.2)$ and low Ursell number), the undertow is
608 weak, and rather vertical-uniform close to the bed. In this region, the undertow
609 is dominated by the outgoing wave field (Figure 16e), which triggers an offshore-
610 directed mean horizontal current. With reducing depth and hence increasing
611 non-linearities (between $x = 35$ m and 50 m) the waves are shoaling and the
612 undertow remains weak and seaward directed. In this region the incoming and
613 outgoing wave field contribute roughly equally to the mean flows ($|\overline{U_{out}}|/|\overline{U_{inc}}| \approx$
614 1 in Figure 16e). As waves propagate closer to the bar crest, the beach becomes
615 much steeper, and the undertow magnitude becomes much stronger, with its
616 maximum reached at mid-depth.

617 The ratio shown in Figure 16e exhibits a narrow band in the lower 10 cm
618 of the water column and seaward of the bar (focussing on the region between
619 $x = 66$ m and 69 m immediately adjacent to the bed where $|\overline{U_{out}}|/|\overline{U_{inc}}| \approx 0.4$)
620 where reflection seems to have an important influence on the undertow. In
621 this narrow band, the mean flow induced by outgoing waves is onshore-directed
622 close to the bed (Figure 16b), and has the effect of almost balancing the offshore-
623 directed mean flow induced by the incoming wave field, leading to almost zero
624 mean flow adjacent to the bed. This is thought to have an influence on bar
625 morphology and will be further discussed in Section 6. Except in this narrow
626 band, the incoming wave field is mostly responsible for the mean return flow
627 around the bar location, indicated by the region where $|\overline{U_{out}}|/|\overline{U_{inc}}|$ is close to
628 zero between $x = 62$ and 72 m.

629 The strengthening of the undertow by the outgoing wave field, can partially
630 be explained by the offshore-oriented Stokes drift that it generates and a change
631 in the wave setup [65]. Indeed, Figure 17a) suggests that the presence of re-
632 flected waves significantly reduces the setdown generated by the breaking of
633 incident waves in the region $x = 72 - 80$ m. Landward and seaward of this
634 region, the setup induced by the outgoing field predominates over that from the

incoming field, which is consistent with the observations made on the undertow (Figure 16d). The undertow is known to influence cross-shore sediment transport, as it plays an important role in the offshore/onshore bar migration [66, 67] and/or in the resuspension of sediment in the water column [68]. Figure 16 for instance suggests that the presence of the outgoing wave field helps to stabilise the bar by weakening the offshore directed mean flow at the bottom of the water column. Although it is consistently offshore-directed, the present results show that the nature of the undertow - at least in reflective environments - is more complex than it was thought before, *e.g.* in terms of temporal structure with a contribution from incident and reflected waves acting with different phasing.

5.2.2. Skewness

Flow skewness and wave asymmetry have been shown by many researchers to contribute to onshore-directed sediment fluxes, therefore balancing the effect that undertow has on surf zone morphodynamics, see for instance Elfrink et al. [15], Elgar et al. [69], Silva et al. [70]. Figure 17b shows the surface elevation asymmetry - defined as $A_s = -\overline{\mathcal{I}m(\mathcal{H}(\eta))^3}/\overline{\eta^2}^{3/2}$ where $\mathcal{I}m$ is the imaginary part of the Hilbert transform \mathcal{H} of the surface elevation - and Figure 17c-e show the flow velocity skewness along the wave flume, computed from the total, incoming and outgoing wave-induced velocity fields. Two striking observations emerge from this analysis: 1) near-zero skewness from the incoming component on top of the bar and on the terrace (Figure 17c), and 2) the negative skewness of the outgoing field (Figure 17d) that therefore generates a negative total skewness over the terrace ($x = 75 - 82$ m, see Figure 17b). The positive skewness seaward of the bar trough and negative skewness landward, along with strong surface elevation asymmetry observed in Figure 17a are thought to explain the 'filling' of the trough observed after the A6-01 test under similar wave conditions [34]. This is consistent with the findings of Grasso et al. [71].

Although, no obvious influence of the multiple quasi-node/antinode system can be observed in the different skewness fields, it is thought to be of importance. Bowen [72] suggested that nodes/antinodes of standing infragravity waves and

665 their associated drift velocities could trigger the generation/migration of bar
 666 towards an equilibrium profile. This was confirmed numerically by Bernabeu
 667 et al. [73] who obtained improved model skill in predicting beach equilibrium
 668 profiles by accounting for wave reflection. Further verification was obtained in
 669 field conditions for sea/swell frequencies by Sánchez-Badorrey et al. [74] who
 670 observed the generation of a multiple bar-trough system in front of a newly
 671 installed seawall which matched the quasi-node/antinode positions of the peak
 672 frequency. Similarly, Alsina et al. [75] observed a reduced offshore bar migration
 673 rate when conditions in the swash were more dissipative: if reflection occurs ear-
 674 lier, the antinode location slightly shifts offshore compared to the location for
 675 a more dissipative swash, generating a different sediment convergent point. Al-
 676 ternatively, this can also be explained by the more intense backwashes observed
 677 that potentially suspend more sediment in the inner surf. Combined with the
 678 stronger undertow under more reflective conditions (Figure 16), it can possibly
 679 promote higher offshore-directed sediment transport rates. As noted by Grasso
 680 et al. [71], despite recent effort in that regard, it is difficult to isolate individual
 681 physical processes that might affect sediment transport rates in the surf zone.
 682 Although rarely considered as such, wave reflection in the sea/swell range of
 683 frequencies in reflective environments is clearly playing a role in the surf zone
 684 hydrodynamics at various time scale, which in turn affect the morphodynamics.

685 6. Conclusions

686 In this paper, a RANS numerical model based on the IHFOAM library [43]
 687 has been validated and used to study the influence of swash-based wave reflection
 688 in the sea/swell range of frequencies on surf zone hydrodynamics at the wave-
 689 by-wave and wave tests temporal scales. A TLS dataset of breaking waves has
 690 been used for the first time to validate the modelled wave shape at various stage
 691 of breaking. This highlighted the important wave-by-wave discrepancies (wave
 692 height and skewness) when using linear theory to retrieve the surface elevation
 693 from the measured pressure signal, close to the break point.

694 The RT was successfully applied to the modelled free surface elevation to
 695 separate incoming and outgoing signals. A wave tracking algorithm was used to
 696 isolate individual waves and demonstrated that reflected waves induce intrawave
 697 variability of individual incident wave properties such as the wave height, and
 698 the wave height to water depth ratio, through the generation of quasi-standing
 699 waves. Variations of up to 35% and 15% are observed for individual and spectral
 700 values of wave height to water depth ratios respectively. This renders the extrac-
 701 tion and the study of incident wave properties more difficult, and must be con-
 702 sidered when parameterising wave reflection in numerical models of nearshore
 703 circulation. By tracking individual reflected waves, a direct link between the
 704 potential energy of swash flows and the reflected wave energy has been demon-
 705 strated. This has two main implications: 1) the potential to use measurements
 706 of swash depths to estimate the energy of individual reflected waves, and 2) a
 707 good representation of swash mass fluxes is required to accurately model surf
 708 zone hydrodynamics [76].

709 Using the Guza84 approach, the incoming and outgoing components of the
 710 modelled horizontal flow velocities were computed along the wave flume in order
 711 to study the contribution of each component to the mean return flow (undertow)
 712 and higher velocity moments (skewness). It was demonstrated that the presence
 713 of strong reflective conditions were promoting the undertow, by strengthening
 714 its magnitude almost everywhere in the wave flume except offshore of the bar
 715 crest, where the outgoing components induce an onshore-directed streaming
 716 close to the bed. This phenomenon, added to the convergence points created
 717 by the observed quasi-standing waves and the influence of reflection on velocity
 718 skewness is thought to influence sediment transport rates and their variation
 719 along the beach profile, contributing to bar generation/migration.

720 **Acknowledgements**

721 This work was supported by the University of Bath, through a URS schol-
 722 arship, and by the EPSRC-funded project EP/N019237/1 "Waves in Shallow

723 Water: A new approach based on high-frequency remote sensing and wave-by-
724 wave analysis". The two anonymous reviewers are greatly acknowledged for
725 their constructive comments on the paper. The BARDEXII data set used in
726 this study is available from www.hydralab.info, and it was obtained with the
727 support by the European Community's 7th Framework Programme through the
728 grant to the budget of the Integrating Activity HYDRALAB IV, contract no.
729 261520.

Table 1: Wave and beach conditions for the different wave tests. For the monochromatic wave tests, H_o was computed as four times the standard deviation of the surface elevation measured at the wave paddle.

Run	H_o (m)	T_p (s)	MSL (m)	β_{surf}	β_{swash}	ξ_{surf}	ξ_{swash}
A1-mono	0.94	8	3.00	1:13	1:11	0.52	0.60
A2-mono	0.71	8	3.00	1:13	1:13	0.58	0.61
A4-mono	0.67	8	3.00	1:14	1:10	0.58	0.83
A6-01	0.70	10.90	2.98	1:12	1:9	0.63	0.97
A6-mono	0.74	12.10	3.00	1:15	1:8	0.64	1.10
A7-mono	0.76	12.10	3.00	1:17	1:8	0.54	1.18
A7T10-mono	-	10	3.00	1:17	1:8	0.49	1.07
A7T11-mono	-	11	3.00	1:17	1:8	0.52	1.12

Table 2: Model skill for reproducing η (PT and TLS), p (PT) , u and v (EMCM): root-mean square error (RMSE), absolute mean error, maximum absolute error and r the linear correlation coefficient (defined as the ratio between the covariance of the two timeseries, and the product of their standard deviation). For conciseness, only minimum and maximum values along the flume are shown, for every modelled quantity and wave test. For the TLS, statistics are calculated only between $x = 70 - 78$ m, whereas for the PT, it concerns the PT positions visible in Figure 1.

Quantity	Run	RMSE	AME	MAE	r^2
$PT - \eta$	A6-mono	0.05-0.08 m	0.04-0.06 m	0.12-0.45 m	0.84-0.98
	A7-mono	0.04-0.06 m	0.03-0.04 m	0.12-0.32 m	0.93-0.98
	A6-01	0.03-0.06 m	0.02-0.04 m	0.15-0.45 m	0.85-0.97
$TLS - \eta$	A6-mono	0.04-0.08 m	0.04-0.06 m	0.10-0.6 m	0.95-0.99
	A7-mono	0.03-0.06 m	0.02-0.04 m	0.09-0.6 m	0.96-0.99
	A6-01	0.06-0.08 m	0.04-0.06 m	0.6-0.8 m	0.85-0.90
p	A6-mono	0.02-0.04 dbar	0.02-0.03 dbar	0.06-0.11 dbar	0.98-0.99
	A7-mono	0.02-0.03 dbar	0.01-0.02 dbar	0.06-0.11 dbar	0.99
	A6-01	0.02-0.04 dbar	0.02-0.03 dbar	0.10-0.24 dbar	0.92-0.97
u	A6-mono	0.06-0.15 m/s	0.05-0.10 m/s	0.18-0.55 m/s	0.89-0.98
	A7-mono	0.04-0.20 m/s	0.03-0.17 m/s	0.11-0.47 m/s	0.97-0.98
	A6-01	0.06-0.27 m/s	0.05-0.20 m/s	0.25-1.90 m/s	0.78-0.96
v	A6-mono	0.02-0.09 m/s	0.02-0.07 m/s	0.12-0.32 m/s	0.38-0.70
	A7-mono	0.02-0.09 m/s	0.02-0.07 m/s	0.06-0.32 m/s	0.47-0.84
	A6-01	0.02-0.12 m/s	0.01-0.07 m/s	0.17-1.52 m/s	0.19-0.21

730 **Figures**

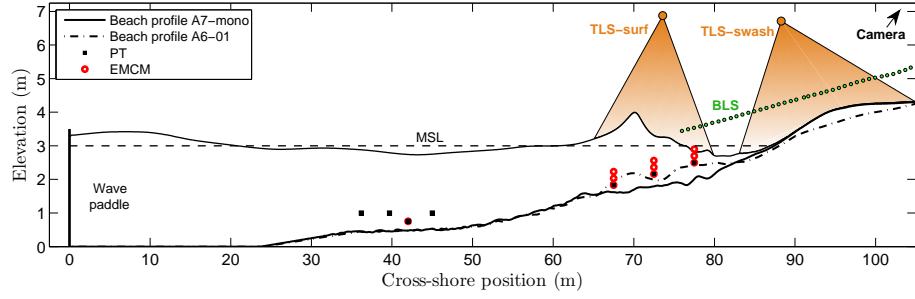


Figure 1: Schematic of the experimental setup for the A6-mono, A7-mono and A6-01 wave tests. The two different initial beach profiles are shown. A dataset from the following instruments was used in the present study: 7 pressure transducers (PT) and electro-magnetic current meters (EMCM) located in the shoaling and surf zones and two terrestrial laser scanners (TLS) deployed at 6.8 and 6.9 m above the flume bed (3.8 and 3.9 mMSL, respectively) within the surf and swash zones. The zones covered by the TLS are indicated with the orange cones.

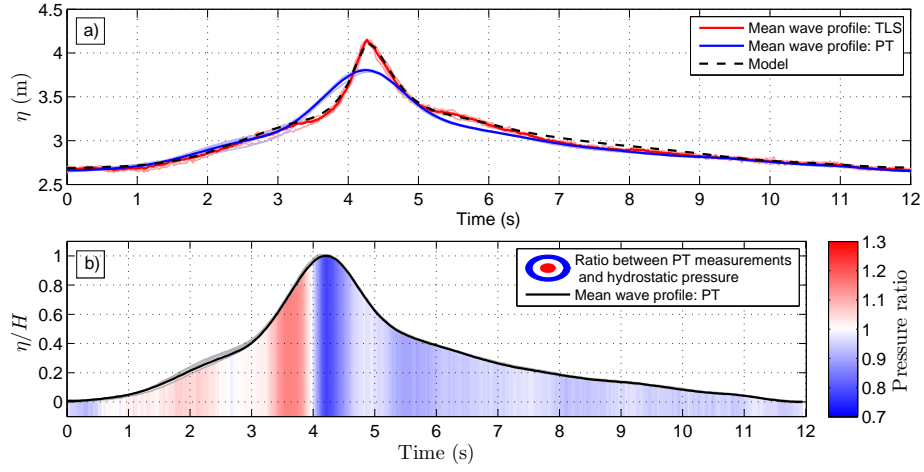


Figure 2: Comparison of individual wave profiles obtained from the surf-zone TLS and the PT, at the PT location $x = 72.5$ m for the A7-mono test. Panel a) shows the wave profile of the modelled waves (light red and blue lines for the TLS and PT, respectively) with the ensemble averaged (thick red and blue lines for the TLS and PT, respectively). The modelled wave profile at that location is also shown as dashed black-line. In panel b), a contour plot of the ratio between the raw measured pressure and hydrostatic pressure based on the surface elevation measured by the TLS is shown: red zones correspond to periods when the pressure is higher than the hydrostatic, and blue zones correspond to periods where it is lower. The ensemble-averaged wave profile is shown as black line, while the gray lines represent individual wave profiles measured by the PT.

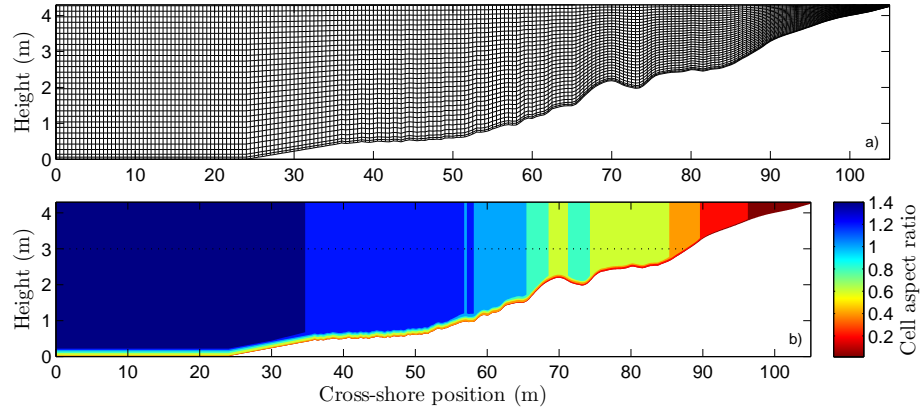


Figure 3: Description of the computational mesh: a) rectangle-based computational mesh for the A6-01 wave test, for visual reasons only every 2nd cell in the vertical direction and 10th cell in the horizontal direction are shown; b) contour plot of the cell aspect ratio.

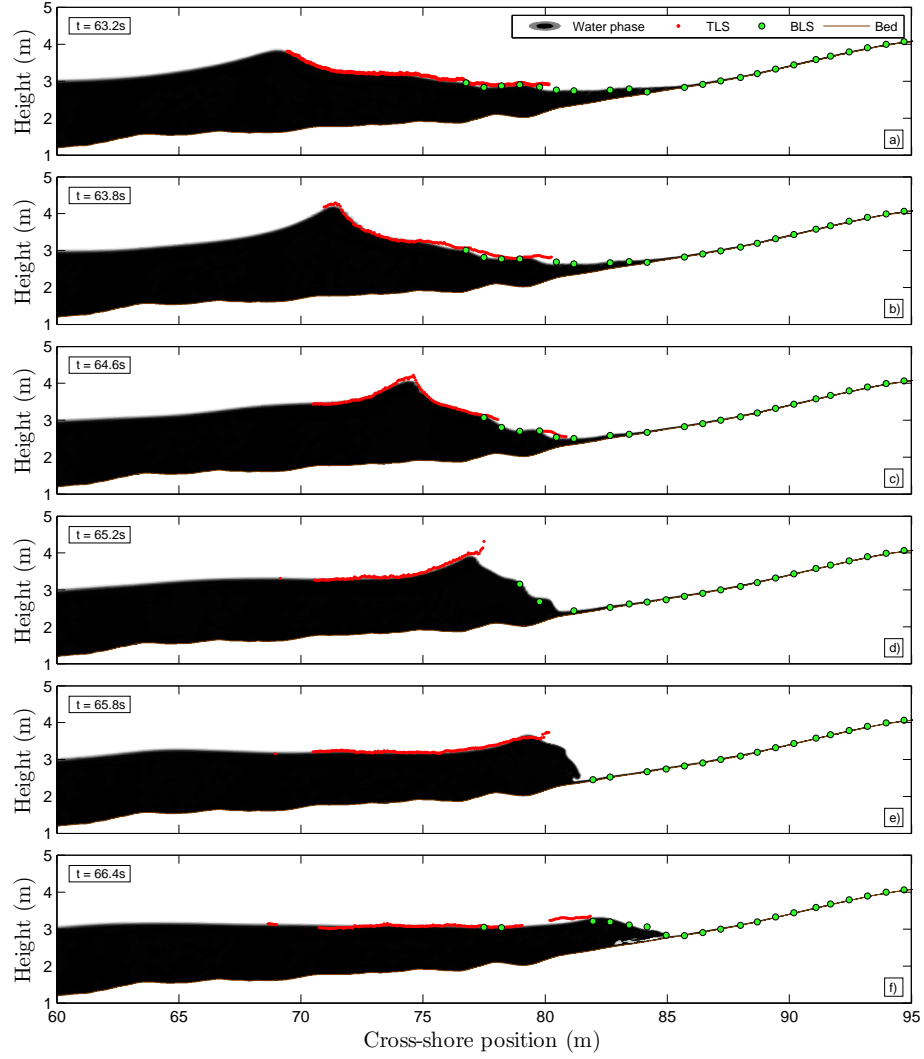


Figure 4: Comparison of the modelled water phase from the A7-mono wave test with the instantaneous free-surface elevation measurements from the TLS and the ultrasonic BLS. Six moments of the breaking process are shown.

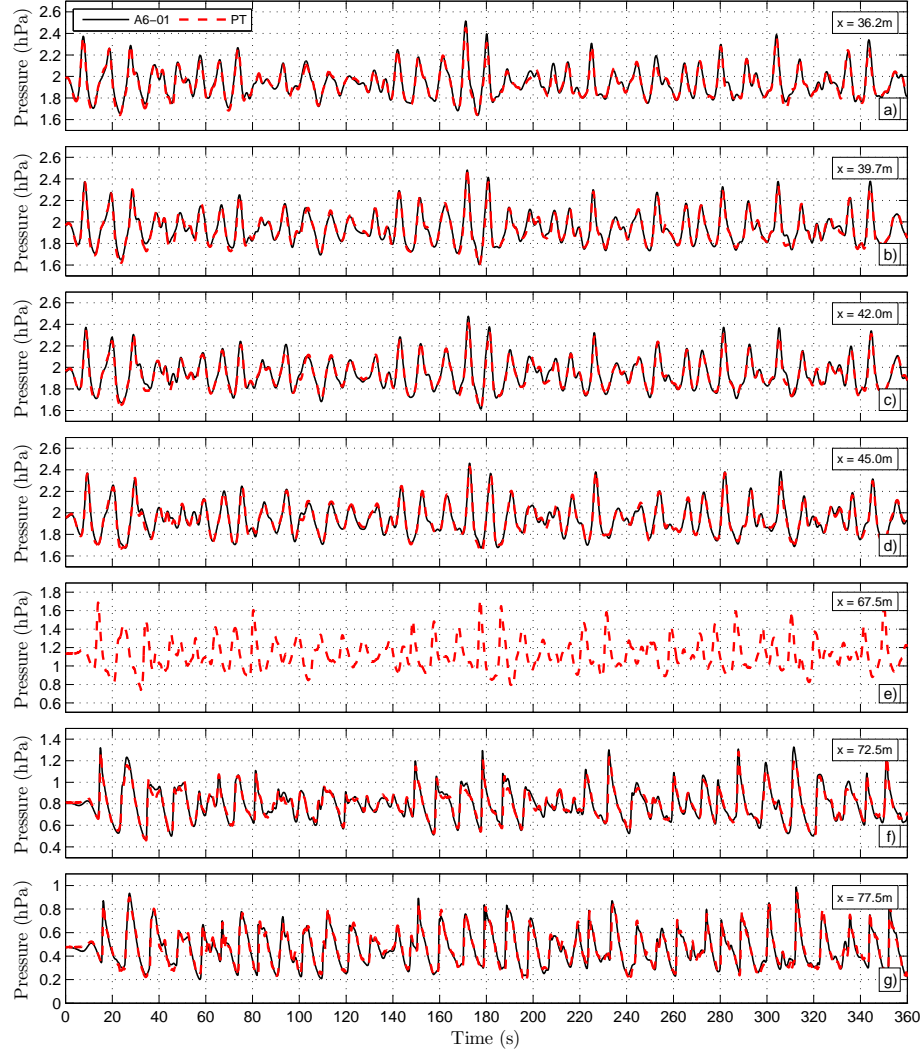


Figure 5: Validation of the modelled relative pressure at the PT locations for the A6-01 wave test, for the first 320s of the simulation. The model and data timeseries are shown at five locations in the shoaling region and two in the surf zone. As seen in Figure 1, the pressure sensor located at $x = 67.5\text{m}$ is slightly buried, the model therefore cannot provide any signal for this location (out of domain).

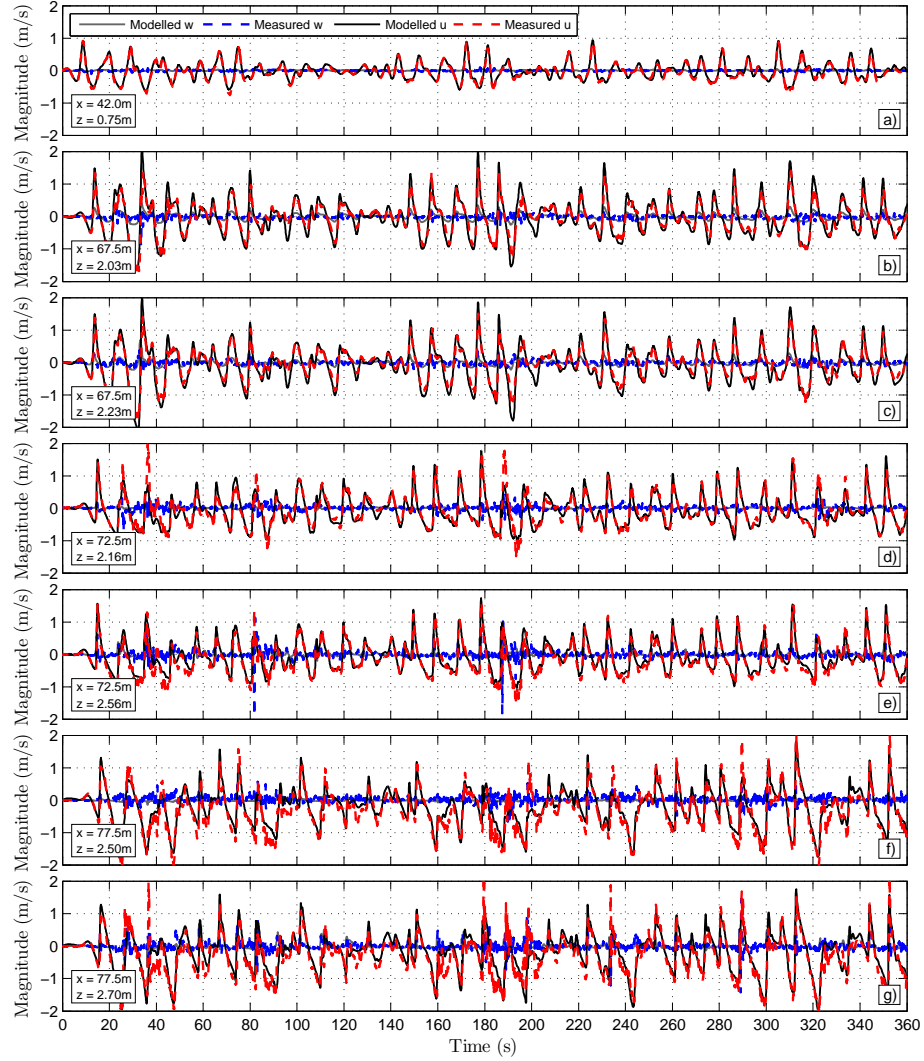


Figure 6: Validation of the modelled hydrodynamics at the EMC locations for the A6-01 wave test, for the first 320 s of the simulation. Modelled horizontal U and vertical V timeseries are shown against measurements at one location in the shoaling region and six in the surf zone.

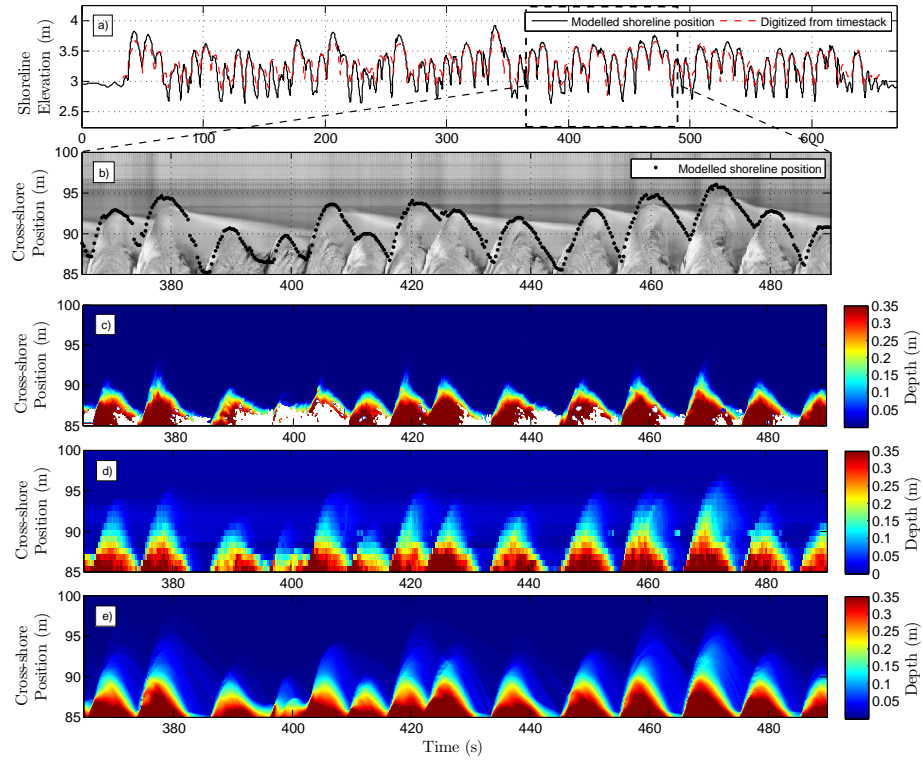


Figure 7: Validation of the model in the swash zone: a) Modelled shoreline elevation and digitised shoreline elevation from the ARGUS video camera timestack are shown for the entire wave test, b) ARGUS Video camera timestack along with the modelled shoreline cross-shore position for a 2 min window, c) Water depths measured by the swash zone TLS, d) Water depths measured by the array of ultrasonic BLS and e) Modelled water depths.

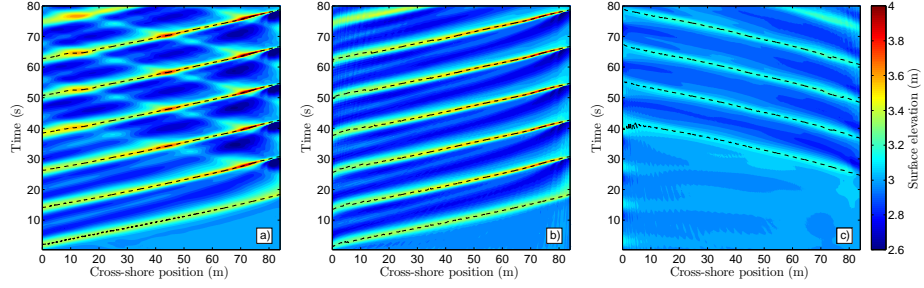


Figure 8: Incoming/outgoing signal separation of the modelled surface elevation using the RT: a) $\eta(x, t)$ diagram of the modelled surface elevation for the A7-mono wave test; b) $\eta_{inc}(x, t)$ diagram of the incoming signal; c) $\eta_{ref}(x, t)$ diagram of the outgoing signal. In every panel, the dashed black lines show the individual waves path, tracked with the methodology presented in Section 4.2.

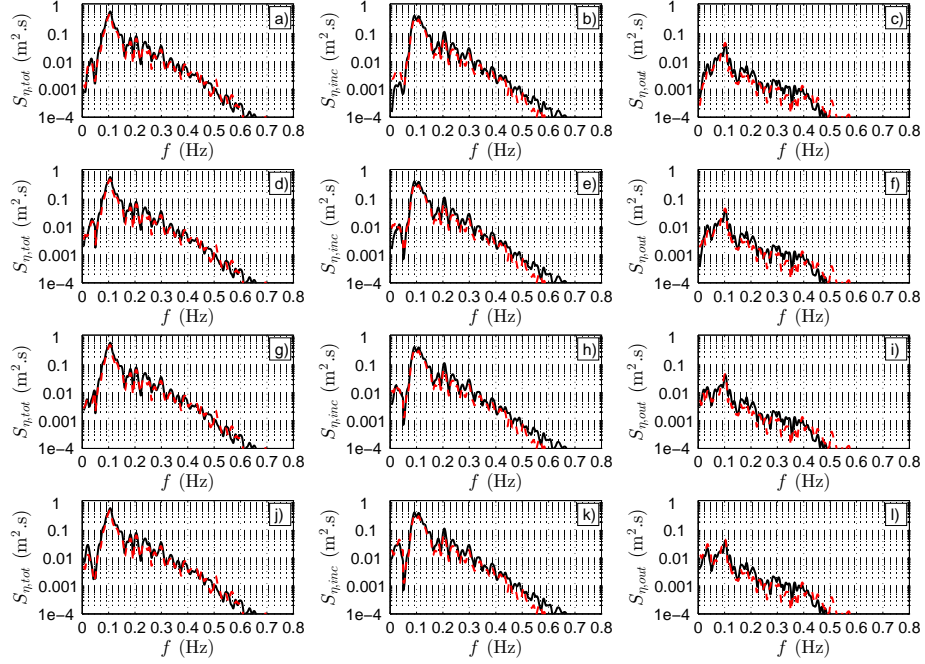


Figure 9: Comparison of the modelled surface elevation spectra (black line) along the wave flume against measurements from pressure-derived data (red dashed line), for total (left column), incoming (central column) and outgoing (right column). The modelled total signal was separated using the RT, while the measured total signal was separated with the Guza84 method. Comparisons are performed at the following cross-shore locations: a-b-c) $x = 42$ m, d-e-f) $x = 67.5$ m, g-h-i) $x = 72.5$ m and j-k-l) $x = 77.5$ m).

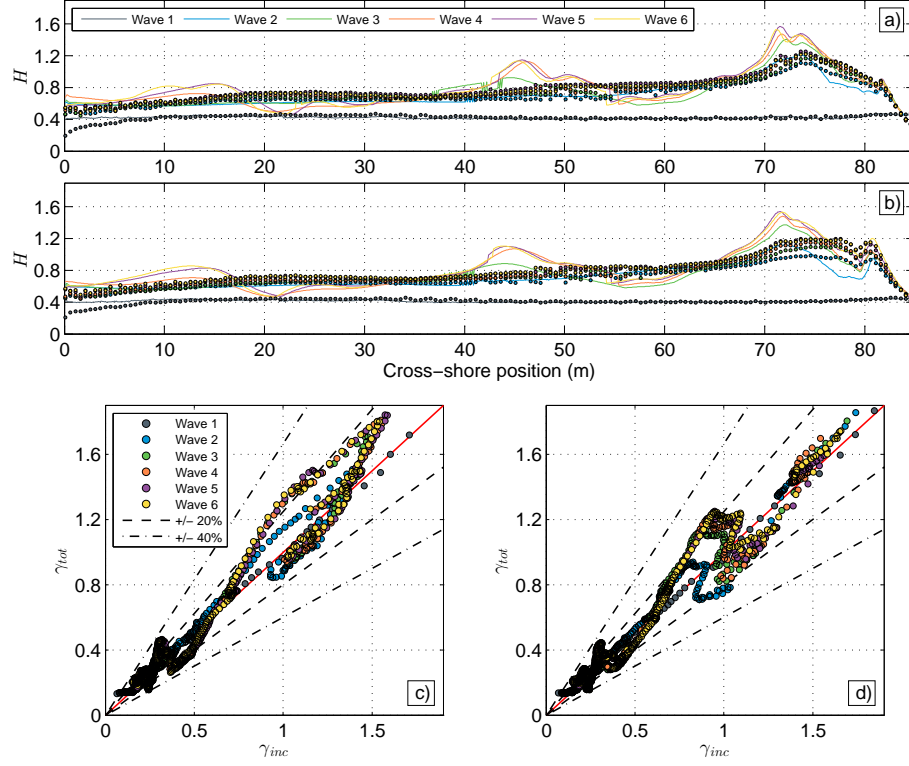


Figure 10: Results from the wave-by-wave analysis on modelled total and incoming signals ($\eta(x, t)$ and $\eta_{inc}(x, t)$) from the A6-mono and A7-mono wave tests. Panels a) and b) represent the wave height evolution extracted from the total (continuous lines) and incoming (dots) signals for the A6-mono and A7-mono wave tests respectively. Panels c) and d) represent the corresponding γ scatter plots for the A6-mono and A7-mono wave tests respectively (values from the total signal against values from incoming signal). In the four panels, the 6 modelled waves are shown, and the same colours are used in the line/dots for the wave numbering; $\pm 20\%$ and $\pm 40\%$ lines are also represented in the scatter plots as dashed and dot-dashed lines respectively.

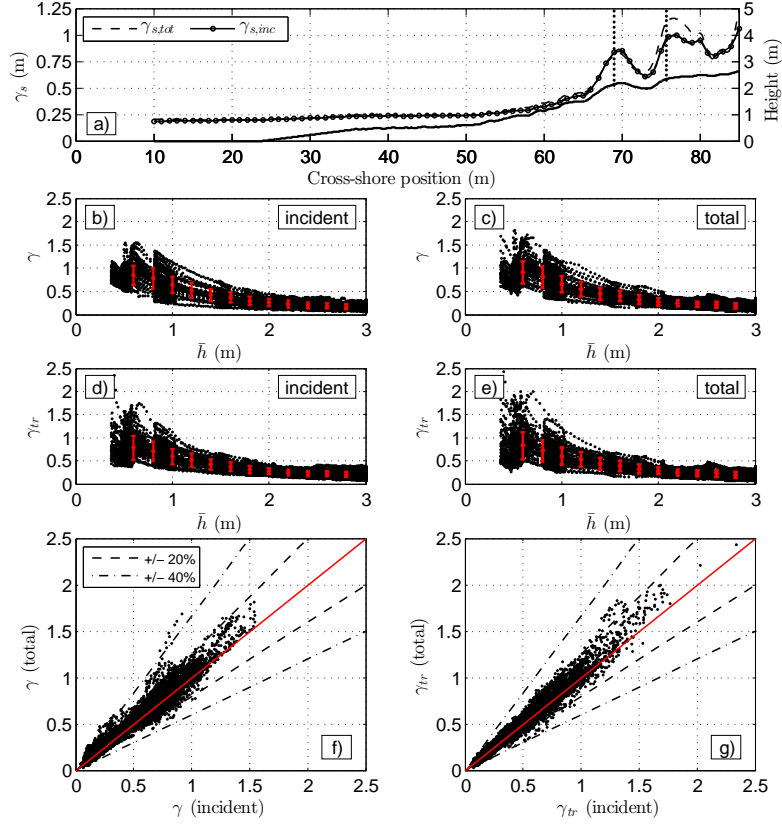


Figure 11: Results from the wave-by-wave analysis on the total and incoming signals ($\eta(x, t)$ and $\eta_{inc}(x, t)$) from the A6-01 irregular wave test. Panel a) shows the cross-shore evolution of the significant wave height to depth ratio γ_s computed from the total (dashed line) and incoming (circled line) signals respectively. The two break points defined as the maximum significant wave height are also shown as vertical dotted lines. Panels b) and c) show the individual γ values computed from the total and incoming signal. Panels d) and e) show the individual γ_{tr} values computed from the total and incoming signal using the water depth below trough h_{tr} . For these 4 scatter plots, standard deviation of the mean are shown as error bars, using bins of 0.2 m. Panels f) and g) represent the corresponding γ and γ_{tr} scatter plots. In these, $\pm 20\%$ and $\pm 40\%$ lines are also represented as dashed and dot-dashed lines respectively.

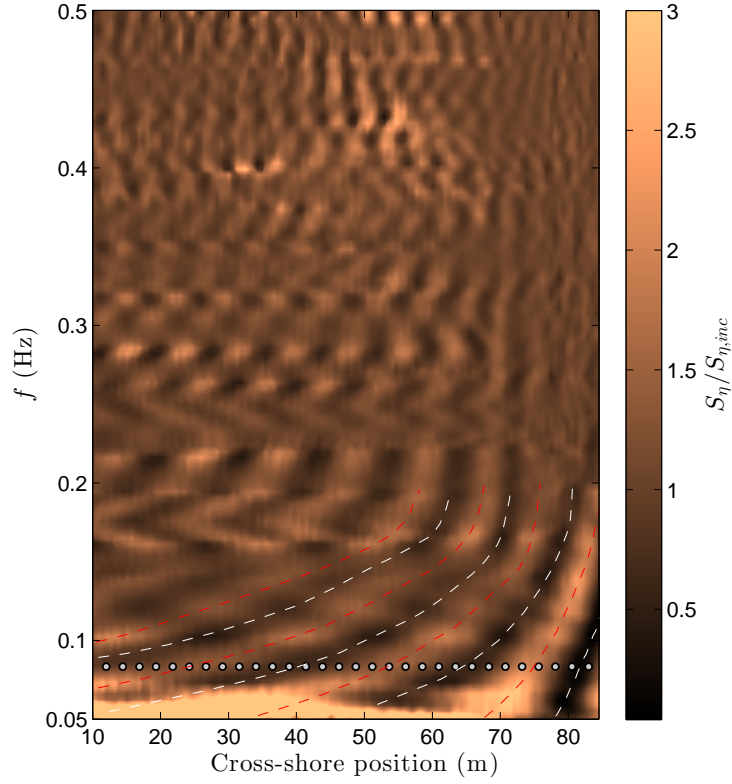


Figure 12: Cross-shore evolution of the ratio of variance density spectra computed on total and incoming surface elevation signals. For $f \leq 0.2$ Hz and for each frequency, the locations of two types of antinodes are shown as white (incident and reflected wave troughs superposed) and red (incident and reflected wave crests superposed) dashed lines. The frequency corresponding to the A6-mono and A7-mono wave tests is also shown by the grey dots.

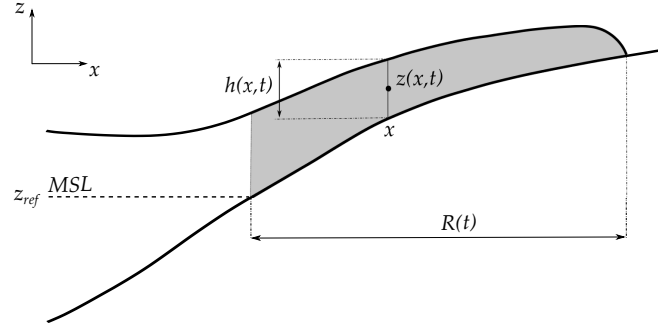


Figure 13: Sketch of a typical swash event, at a time t . Mean Sea Level (MSL) defines the elevation reference z_{ref} for the potential energy definition in Equation 6. The intersection between MSL and the bed also defines the origin to estimate the time-varying horizontal shoreline position $R(t)$. x defines the cross-shore location, $h(x, t)$ the water depth at x and time t , $z(x, t)$ the middle point of the water column at x .

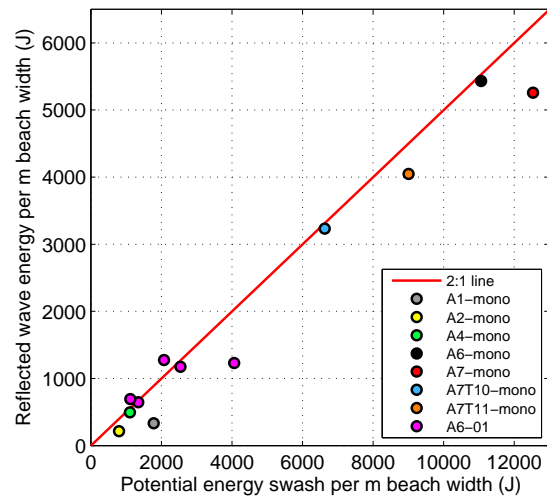


Figure 14: Comparison between reflected wave energy (Equation 5) and maximum potential energy in the preceding swash event (Equation 6) for a range of validated and unvalidated test cases detailed in Table 1.

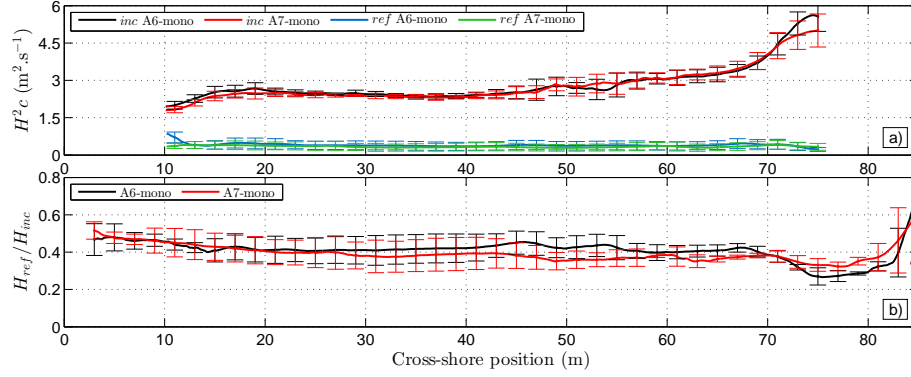


Figure 15: Cross-shore evolution of reflection coefficient based on individual wave properties: a) individual wave incident and reflected energy fluxes and b) individual incident and reflected wave height ratio for the A6-mono and A7-mono tests. The value for each run represents the ensemble-average of the four first waves, since only four reflected waves could be tracked (as seen in Figure 2c). Standard deviation of the ensemble-average values are shown every two meters in the cross-shore direction, as error bars. For the fluxes expression, wave celerity was estimated for each wave on an individual basis, using the tracking method described in Section 3.2.

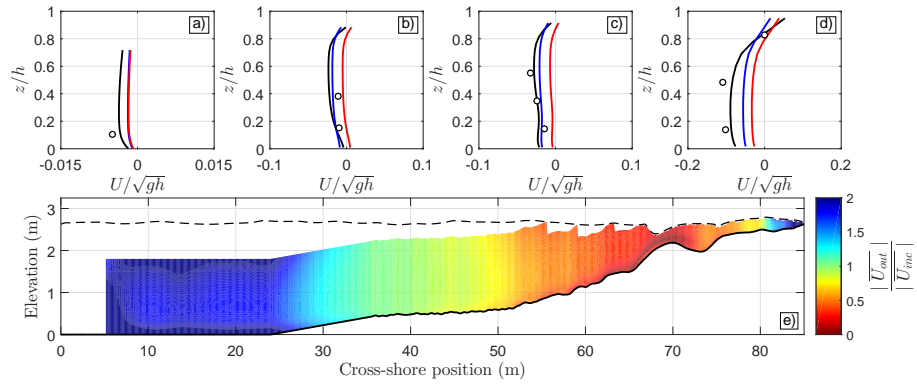


Figure 16: Vertical structure of the modelled undertow along the flume for the A6-01 wave test. The top panels show the modelled undertow from total (black line), incoming (blue line) and outgoing (red line) signals at: a) $x = 42$ m, b) $x = 67.5$ m, c) $x = 72.5$ m and d) $x = 77.5$ m. Experimental data from the EMCM are shown as circles. Panel e) shows a contour plot of the outgoing signal contribution on the undertow structure, compared to the incoming contribution. The black dashed line corresponds to the minimum surface elevation reached, and any data from above that limit has been removed to not bias the time-average.

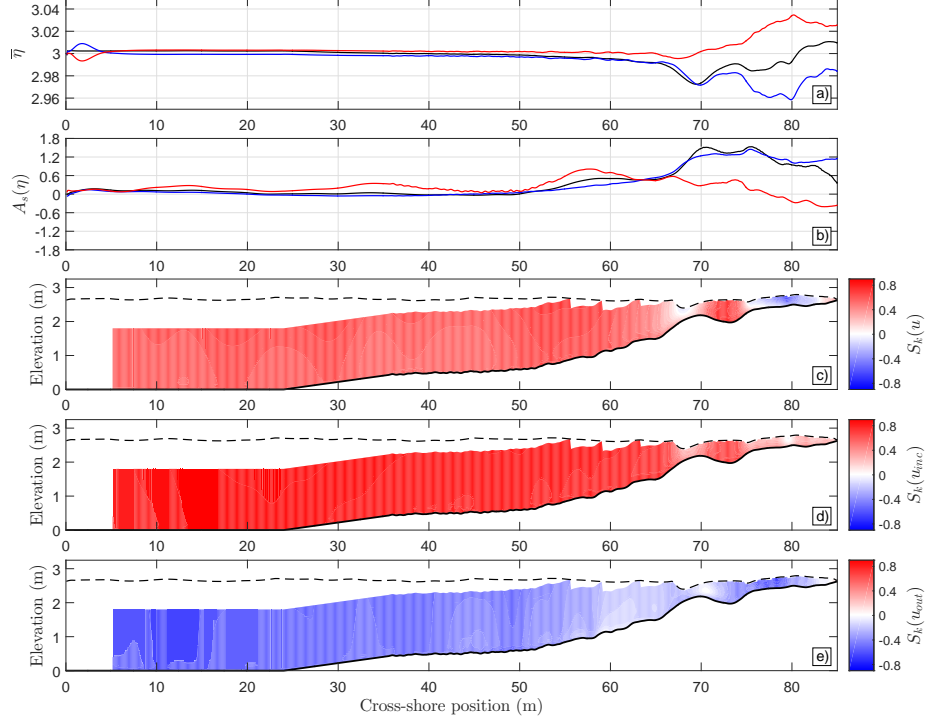


Figure 17: Evolution of modelled time-averaged surf zone parameters along the wave flume. Panel a) shows the modelled time-averaged surface elevation (wave setup) for the total, incoming and outgoing signal (black, blue and red lines respectively). Panel b) shows the surface elevation asymmetry for the total, incoming and outgoing signal (black, blue and red lines respectively). Panels c), d) and e) show contour plots of the skewness computed from the total, incoming and outgoing horizontal velocity fields, respectively. The black dashed line in panels c-e) corresponds to the minimum surface elevation reached, and any data from above that limit has been removed to not bias the skewness computation.

731 References

- 732 [1] J. R. Miles, P. E. Russell, D. A. Huntley, Field measurements of sediment
733 dynamics in front of a seawall, *Journal of Coastal Research* 17 (2001)
734 195–206.
- 735 [2] M. Brocchini, T. E. Baldock, Recent advances in modeling swash zone
736 dynamics: Influence of surf-swash interaction on nearshore hydrodynam-
737 ics and morphodynamics, *Reviews of Geophysics* 46 (2008). doi:10.1029/
738 2006RG000215.
- 739 [3] B. Zanuttigh, J. W. van der Meer, Wave reflection from coastal structures
740 in design conditions, *Coastal Engineering* 55 (2008) 771–779. doi:10.1016/
741 j.coastaleng.2008.02.009.
- 742 [4] C. R. Iribarren, C. Nogales, Protection des ports, *XVIIth International*
743 *Navigation Congres* 1 (1949).
- 744 [5] A. Miche, Le pouvoir réfléchissant des ouvrages maritimes exposés à l’action
745 de la houle, *Annales des Ponts et Chaussées* 121 (1951) 285–319.
- 746 [6] J. A. Battjes, Surf similarity, in: *Proceedings of the 14th Conference on*
747 *Coastal Engineering*, Copenhagen, Denmark, 1974, pp. 466–480.
- 748 [7] S. A. Hughes, J. E. Fowler, Estimating wave-induced kinematics at sloping
749 structures, *Journal of waterway, port, coastal, and ocean engineering* 121
750 (1995) 209–215.
- 751 [8] J. R. Miles, P. E. Russell, Dynamics of a reflective beach with a low tide
752 terrace, *Continental Shelf Research* 24 (2004) 1219–1247. doi:10.1016/j.
753 csr.2004.03.004.
- 754 [9] A. Baquerizo, M. A. Losada, J. M. Smith, N. Kobayashi, Cross-shore vari-
755 ation of wave reflection from beaches, *Journal of waterway, port, coastal,*
756 *and ocean engineering* 123 (1997) 274–279.

- 757 [10] S. Elgar, R. T. Guza, Observations of bispectra of shoaling surface grav-
758 ity waves, *Journal of Fluid Mechanics* 161 (1985) 425–448. doi:10.1017/
759 S0022112085003007.
- 760 [11] A. T. M. de Bakker, T. H. C. Herbers, P. B. Smit, M. F. S. Tissier,
761 B. G. Ruessink, Nonlinear infragravitywave interactions on a gently sloping
762 laboratory beach, *Journal of Physical Oceanography* 45 (2015) 589–605.
763 doi:10.1175/JPO-D-14-0186.1.
- 764 [12] A. Sheremet, R. T. Guza, S. Elgar, T. H. C. Herbers, Observations of
765 nearshore infragravity waves: Seaward and shoreward propagating compo-
766 nents, *Journal of Geophysical Research: Oceans* 107 (2002) 10–1–10–10.
767 doi:10.1029/2001JC000970.
- 768 [13] S. Elgar, T. H. C. Herbers, R. T. Guza, Reflection of ocean surface gravity
769 waves from a natural beach, *Journal of Physical Oceanography* 24 (1994)
770 1503–1511. doi:10.1175/1520-0485(1994)024<1503:R00SGW>2.0.CO;2.
- 771 [14] R. Almar, P. Catalan, R. Ibaceta, C. Blenkinsopp, R. Cienfuegos, M. Vil-
772 lagran, J. C. Aguilera, B. Castelle, Swash zone based reflection during
773 energetic wave conditions at a dissipative beach: Toward a wave-by-wave
774 approach, in: *Proceedings of the 34th Conference on Coastal Engineering*,
775 Seoul, Korea, 2014.
- 776 [15] B. Elfrink, K. A. Rakha, R. Deigaard, I. Brøker, Effect of near-bed velocity
777 skewness on cross shore sediment transport, in: *Proceedings of the 4th*
778 *International Symposium on Coasting Engineering and Science of Coastal*
779 *Sediment Processes (ASCE)*, Hauppauge, New York, United States, 1999,
780 pp. 33–47.
- 781 [16] J. C. Doering, B. Elfrink, D. M. Hanes, B. G. Ruessink, Parameterization
782 of velocity skewness under waves and its effect on cross-shore sediment
783 transport, in: *Proceedings of the 27th Conference on Coastal Engineering*,
784 Sydney, Australia, 2000, pp. 1383–1397.

- 785 [17] M. A. Hoque, T. Asano, M. A. L. Neshaei, Effect of reflective structures
786 on undertow distribution, in: Proceedings of the Fourth International
787 Symposium on Ocean Wave Measurement and Analysis, Waves 2001, San
788 Francisco, California, United States, 2002, pp. 1042–1051. doi:10.1061/
789 40604(273)106.
- 790 [18] J. A. Battjes, J. P. F. M. Janssen, Energy loss and set-up due to break-
791 ing of random waves, in: Proceedings of the 16th Conference on Coastal
792 Engineering, Hamburg, Germany, 1978, pp. 569–587.
- 793 [19] B. Raubenheimer, R. Guza, S. Elgar, Wave transformation across the inner
794 surf zone, *Journal of Geophysical Research: Oceans* 101 (1996) 25589–
795 25597.
- 796 [20] N. Sénéchal, Etude de la propagation des vagues au-dessus d’une
797 bathymétrie complexe en zone de surf, Ph.D. thesis, École doctorale sci-
798 ences du Vivant, géosciences, sciences de l’environnement, Université de
799 Bordeaux I, 2003.
- 800 [21] K. Martins, C. E. Blenkinsopp, J. Zang, Monitoring individual wave char-
801 acteristics in the inner surf with a 2-dimensional laser scanner (LiDAR),
802 *Journal of Sensors*, 2016 (2016) 1–11. doi:10.1155/2016/7965431.
- 803 [22] R. Almar, R. Ibaceta, C. Blenkinsopp, P. Catalan, R. Cienfuegos, N. Viet,
804 D. Thuan, D. V. UU, J.-P. Lefebvre, W. Laryea, et al., Swash-based wave
805 energy reflection on natural beaches, in: *Coastal Sediments 2015: The*
806 *Proceedings of the Coastal Sediments 2015*, World Scientific, 2015.
- 807 [23] K. Inch, M. Davidson, G. Masselink, P. Russell, Accurate estimation of
808 wave reflection on a high energy, dissipative beach, *Journal of Coastal*
809 *Research SI* 75 (2016) 877–881.
- 810 [24] R. Kajima, Estimation of incident wave spectrum in the sea area influenced
811 by reflection, in: *Proceedings of Coastal Engineering in Japan*, Vol. 12,
812 1969, pp. 9–16.

- [25] E. B. Thornton, R. J. Calhoun, Spectral resolution of breakwater reflected waves, *Journal of the Waterways, Harbors and Coastal Engineering Division* 98 (1972) 443–460.
- [26] Y. Goda, T. Suzuki, Estimation of incident and reflected waves in random wave experiments, in: *Proceedings of the 15th Conference on Coastal Engineering*, Copenhagen, Denmark, 1976, pp. 828–845.
- [27] E. P. D. Mansard, E. R. Funke, The measurement of incident and reflected spectra using a least squares method, in: *Proceedings of the 17th Conference on Coastal Engineering*, Sydney, Australia, 1980, pp. 154–172.
- [28] J. A. Zelt, J. E. Skjelbreia, Estimating incident and reflected wave fields using an arbitrary number of wave gauges, in: *Proceedings of the 23rd Conference on Coastal Engineering*, Venice, Italy, 1992, pp. 777–789.
- [29] C.-Y. Lin, C.-J. Huang, Decomposition of incident and reflected higher harmonic waves using four wave gauges, *Coastal Engineering* 51 (2004) 395–406. doi:10.1016/j.coastaleng.2004.04.004.
- [30] R. T. Guza, A. J. Bowen, Resonant interactions for waves breaking on a beach, in: *Proceedings of the 15th Conference on Coastal Engineering*, Honolulu, Hawaii, 1976, pp. 560–579.
- [31] R. T. Guza, E. B. Thornton, R. A. Holman, Swash on steep and shallow beaches, in: *Proceedings of the 19th Conference on Coastal Engineering*, Houston, Texas, 1984, pp. 708–723.
- [32] R. Almar, H. Michallet, R. Cienfuegos, P. Bonneton, M. Tissier, G. Ruessink, On the use of the radon transform in studying nearshore wave dynamics, *Coastal Engineering* 92 (2014) 24–30. doi:10.1016/j.coastaleng.2014.06.008.
- [33] R. Almar, P. Bonneton, H. Michallet, R. Cienfuegos, B. G. Ruessink, M. Tissier, On the use of the radon transform in studying wave dynam-

- 840 ics, in: Coastal Dynamics '13: Proceedings of the Seventh Conference on
841 Coastal Dynamics, Arcachon, France, 2013, pp. 73–82.
- 842 [34] G. Masselink, A. Ruju, D. Conley, I. Turner, G. Ruessink, A. Matias,
843 C. Thompson, B. Castelle, J. Puleo, V. Citerone, G. Wolters, Large-scale
844 Barrier Dynamics Experiment II (*BARDEX II*): Experimental design, in-
845 strumentation, test program, and data set, Coastal Engineering 113 (2016)
846 3 – 18. doi:10.1016/j.coastaleng.2015.07.009.
- 847 [35] C. T. Bishop, M. A. Donelan, Measuring waves with pressure transduc-
848 ers, Coastal Engineering 11 (1987) 309–328. doi:10.1016/0378-3839(87)
849 90031-7.
- 850 [36] K. Inch, Surf zone hydrodynamics: Measuring waves and currents, in:
851 Geomorphological Techniques, Chap. 3, Sec. 2.3, British Society of Geo-
852 morphology, 2014.
- 853 [37] M. O. Green, Test of sediment initial-motion theories using irregular-wave
854 field data, Sedimentology 46 (1999) 427–441. doi:10.1046/j.1365-3091.
855 1999.00221.x.
- 856 [38] P. Nielsen, Local approximations : A new way of dealing with irregular
857 waves, in: Proceedings of the 20th Conference on Coastal Engineering,
858 Taipei, Taiwan, 1986, pp. 633–646.
- 859 [39] M. Townsend, J. D. Fenton, A comparison of analysis methods for wave
860 pressure data, in: Proceedings of the 25th Conference on Coastal Engi-
861 neering, Orlando, Florida, 1996, pp. 575–588.
- 862 [40] C. H. Barker, R. J. Sobey, Irregular wave kinematics from a pressure record,
863 in: Proceedings of the 25th Conference on Coastal Engineering, Orlando,
864 Florida, 1996, pp. 1034–1047.
- 865 [41] M. J. F. Stive, Velocity and pressure field of spilling breakers, in: Pro-
866 ceedings of the 17th Conference on Coastal Engineering, Sydney, Australia,
867 1980, pp. 547–566.

- [42] I. L. Turner, P. E. Russell, T. Butt, Measurement of wave-by-wave bed-levels in the swash zone, *Coastal Engineering* 55 (2008) 1237–1242. doi:10.1016/j.coastaleng.2008.09.009.
- [43] P. Higuera, J. L. Lara, I. J. Losada, Realistic wave generation and active wave absorption for Navier-Stokes models: Application to OpenFOAM®, *Coastal Engineering* 71 (2013) 102–118. doi:10.1016/j.coastaleng.2012.07.002.
- [44] N. G. Jacobsen, J. Fredsoe, J. H. Jensen, Formation and development of a breaker bar under regular waves. part 1: Model description and hydrodynamics, *Coastal Engineering* 88 (2014) 182–193. doi:10.1016/j.coastaleng.2013.12.008.
- [45] R. G. Dean, R. A. Dalrymple, *Water wave mechanics for engineers and scientists*, Advanced Series on Ocean Engineering: Volume 2, World Scientific, 1991.
- [46] E. Berberović, N. P. van Hinsberg, S. Jakirlić, I. V. Roisman, C. Tropea, Drop impact onto a liquid layer of finite thickness: Dynamics of the cavity evolution, *Phys. Rev. E* 79 (2009) 036306. doi:10.1103/PhysRevE.79.036306.
- [47] F. R. Menter, Two-equation eddy-viscosity turbulence models for engineering applications, *AIAA Journal* 32 (1994) 1598–1605. doi:10.2514/3.12149.
- [48] S. A. Brown, V. Magar, D. M. Greaves, D. C. Conley, An evaluation of rans turbulence closure models for spilling breakers, in: *Proceedings of the 34th Conference on Coastal Engineering*, Seoul, Korea, 2014.
- [49] J. Z. Gailani, S. J. Smith, *Sediment Transport Analysis from OBS/EMCM During Storms*, Technical Report, DTIC Document, 2000.

- [50] S. Elgar, B. Raubenheimer, R. T. Guza, Quality control of acoustic doppler velocimeter data in the surfzone, *Measurement Science and Technology* 16 (2005) 1889. doi:10.1088/0957-0233/16/10/002.
- [51] Z.-C. Huang, K.-S. Hwang, Measurements of surface thermal structure, kinematics, and turbulence of a large-scale solitary breaking wave using infrared imaging techniques, *Coastal Engineering* 96 (2015) 132–147. doi:10.1016/j.coastaleng.2014.12.005.
- [52] C. E. Blenkinsopp, J. R. Chaplin, Void fraction measurements and scale effects in breaking waves in freshwater and seawater, *Coastal Engineering* 58 (2011) 417–428. doi:10.1016/j.coastaleng.2010.12.006.
- [53] B. Hofland, E. Diamantidou, P. van Steeg, P. Meys, Wave runup and wave overtopping measurements using a laser scanner, *Coastal Engineering* 106 (2015) 20 – 29. doi:10.1016/j.coastaleng.2015.09.003.
- [54] J. Radon, Über die Bestimmung von Funktionen durch ihre Integralwerte längs gewisser Mannigfaltigkeiten, *Akad. Wiss.* 69 (1917) 262–277.
- [55] J. R. Miles, P. E. Russell, D. A. Huntley, Sediment transport and wave reflection near a seawall, in: *Proceedings of the 25th Conference on Coastal Engineering*, Orlando, Florida, 1996, pp. 2612–2624.
- [56] H. E. Power, M. G. Hughes, T. Aagaard, T. E. Baldock, Nearshore wave height variation in unsaturated surf, *Journal of Geophysical Research: Oceans* 115 (2010). doi:10.1029/2009JC005758.
- [57] H. E. Power, M. G. Hughes, T. E. Baldock, A novel method for tracking individual waves in the surf zone, *Coastal Engineering* 98 (2015) 26–30. doi:10.1016/j.coastaleng.2015.01.006.
- [58] M. Postacchini, M. Brocchini, A wave-by-wave analysis for the evaluation of the breaking-wave celerity, *Applied Ocean Research* 46 (2014) 15–27. doi:10.1016/j.apor.2014.01.005.

- 921 [59] G. C. J. Morgan, J. Zang, D. Greaves, A. Heath, C. Whitlow, J. Young,
922 Using the rasInterFoam CFD model for wave transformation and coastal
923 modelling, in: Proceedings of the 32nd Conference on Coastal Engineering,
924 Shanghai, China, 2010.
- 925 [60] L. P. Almeida, G. Masselink, P. E. Russell, M. A. Davidson, Observa-
926 tions of gravel beach dynamics during high energy wave conditions us-
927 ing a laser scanner, *Geomorphology* 228 (2015) 15–27. doi:10.1016/j.
928 geomorph.2014.08.019.
- 929 [61] A. Baquerizo, M. A. Losada, J. M. Smith, Wave reflection from beaches:
930 A predictive model, *Journal of Coastal Research* 14 (1998) 291–298.
- 931 [62] I. J. Mario-Tapia, P. E. Russell, T. J. O’Hare, M. A. Davidson, D. A.
932 Huntley, Cross-shore sediment transport on natural beaches and its relation
933 to sandbar migration patterns: 1. field observations and derivation of a
934 transport parameterization, *Journal of Geophysical Research: Oceans* 112
935 (2007). doi:10.1029/2005JC002893.
- 936 [63] B. Robertson, K. Hall, Z. Richard, I. Nistor, Breaking waves: Review
937 of characteristic relationships, *Coastal Engineering Journal* 55 (2013)
938 1350002. doi:10.1142/S0578563413500022.
- 939 [64] U. Putrevu, I. A. Svendsen, Vertical structure of the undertow outside
940 the surf zone, *Journal of Geophysical Research: Oceans* 98 (1993) 22707–
941 22716. doi:10.1029/93JC02399.
- 942 [65] F. J. Mendez, I. J. Losada, R. A. Dalrymple, M. A. Losada, Effects of wave
943 reflection and dissipation on wave-induced second order magnitudes, in:
944 Proceedings of the 26th Conference on Coastal Engineering, Copenhagen,
945 Denmark, 1998, pp. 537–500.
- 946 [66] M. Dyhr-Nielson, T. Sørensen, Some sand transport phenomena on coasts
947 with bars, in: Proceedings of the 12th Conference on Coastal Engineering,
948 Washington, D.C., 1970, pp. 855–865.

- [67] E. B. Thornton, R. T. Humiston, W. Birkemeier, Bar/trough generation on a natural beach, *Journal of Geophysical Research: Oceans* 101 (1996) 12097–12110. doi:10.1029/96JC00209.
- [68] J. Fredsøe, R. Deigaard, *Mechanics of coastal sediment transport*, Advanced Series on Ocean Engineering: Volume 3, World Scientific, 1992.
- [69] S. Elgar, E. L. Gallagher, R. T. Guza, Nearshore sandbar migration, *Journal of Geophysical Research: Oceans* 106 (2001) 11623–11627. doi:10.1029/2000JC000389.
- [70] P. A. Silva, T. Abreu, D. A. van der A, F. Sancho, B. G. Ruessink, J. van der Werf, J. S. Ribberink, Sediment transport in nonlinear skewed oscillatory flows: Transkew experiments, *Journal of Hydraulic Research* 49 (2011) 72–80. doi:10.1080/00221686.2011.592681.
- [71] F. Grasso, H. Michallet, E. Barthlemy, Sediment transport associated with morphological beach changes forced by irregular asymmetric, skewed waves, *Journal of Geophysical Research: Oceans* 116 (2011). doi:10.1029/2010JC006550, c03020.
- [72] A. J. Bowen, Simple models of nearshore sedimentation, beach profiles and longshore bars, *The Coastline of Canada*, Geological Survey of Canada (1980) 1–11.
- [73] A. M. Bernabeu, R. Medina, C. Vidal, Wave reflection on natural beaches: an equilibrium beach profile model, *Estuarine, Coastal and Shelf Science* 57 (2003) 577–585. doi:10.1016/S0272-7714(02)00393-1.
- [74] E. Sánchez-Badorrey, M. A. Losada, J. Rodero, Sediment transport patterns in front of reflective structures under wind wave-dominated conditions, *Coastal Engineering* 55 (2008) 685–700. doi:10.1016/j.coastaleng.2007.11.005.
- [75] J. M. Alsina, I. Cáceres, M. Brocchini, T. E. Baldock, An experimental study on sediment transport and bed evolution under different swash zone

- 977 morphological conditions, Coastal Engineering 68 (2012) 31–43. doi:10.
978 1016/j.coastaleng.2012.04.008.
- 979 [76] A. Torres-Freyermuth, J. L. Lara, I. J. Losada, Numerical modelling of
980 short- and long-wave transformation on a barred beach, Coastal Engineer-
981 ing 57 (2010) 317–330. doi:10.1016/j.coastaleng.2009.10.013.